Teleconnections Governing the Interannual Variability of Great Plains Low-Level Jets in May

Shubhi Agrawal*, Craig R. Ferguson

Atmospheric Sciences Research Center, and Department of Atmospheric and Environmental Sciences, University at Albany, New York

Lance Bosart

Department of Atmospheric and Environmental Sciences, University at Albany, New York

D. Alex Burrows

Atmospheric Sciences Research Center, and Department of Atmospheric and Environmental Sciences, University at Albany, New York

**Corresponding author*: Shubhi Agrawal, sagrawal2@albany.edu

ABSTRACT

A spectral analysis of Great Plains 850-hPa meridional winds (V850) from ECMWF′s coupled climate reanalysis of 1901-2010 (CERA-20C) reveals that their warm season (April-September) interannual variability peaks in May with 2-6 year periodicity, suggestive of an underlying teleconnection influence on low-level jets (LLJs). Using an objective, dynamical jet classification framework based on 500-hPa wave activity, we pursue a large scale teleconnection hypothesis separately for LLJs that are uncoupled (LLJUC) and coupled (LLJC) to the upper-level jet stream. Differentiating between jet types enables isolation of their respective sources of variability. In the South Central Plains (SCP), May LLJCs account for nearly 1.6 times more precipitation and 1.5 times greater V850 compared to LLJUCs. Composite analyses of May 250-hPa geopotential height (Z250) conditioned on LLJC and LLJUC frequencies highlight a distinct planetary-scale Rossby wave pattern with wavenumber-five, indicative of an underlying Circumglobal Teleconnection (CGT). An index of May CGT is found to be significantly correlated with both LLJC ($r = 0.62$) and LLJUC ($r = -0.48$) frequencies. Additionally, a significant correlation is found between May LLJUC frequency and NAO ($r = 0.33$). Further analyses expose decadal scale variations in the CGT-LLJC(LLJUC) teleconnection that are linked to the PDO. Dynamically, these large scale teleconnections impact LLJ class frequency and intensity via upper-level geopotential anomalies over the western U.S. that modulate near-surface geopotential and temperature gradients across the SCP.

1. Introduction

Warm season (April-September) precipitation in the Great Plains is highly variable from year to year (e.g., Ferguson et al. 2018; Christian et al. 2015) and not always predictable (e.g., Hoerling et al. 2014). The lack of predictability is concerning because the region accounts for a large fraction of U.S. agricultural (e.g., Basara et al. 2013; Melillo et al. 2014) and wind energy (AWEA 2018) production. Historically, several potential sources of precipitation predictability at seasonal to decadal time scales have been investigated, including internal atmospheric variability (e.g., Hoerling et al. 2014), eastward propagating short waves over North America (e.g., Wang et al. 2013; Jiang et al. 2006) and the Circumglobal teleconnection (CGT; e.g., Ding and Wang 2005), ridge building and concomitant surface temperature anomalies over the western U.S. (e.g., Xue et al. 2012, 2016, 2018), Pacific and Atlantic SST teleconnections (e.g., Trenberth et al. 1988; Yang et al. 2007; Hoerling et al. 2009; Mo et al. 2009; Wang et al. 2010a; Hu et al. 2011; Dai 2013; Kam et al. 2014), and the East Asia–Pacific–North America teleconnection (e.g., Lau and Weng 2002; Lau et al. 2004; Li et al. 2005; Zhu and Li 2016). To the extent that nearly 70% of summer atmospheric moisture influx and more than half of summer precipitation is associated with Great Plains southerly low-level jets (LLJs; e.g., Bonner 1968; Whiteman et al. 1997; Algarra et al. 2019), the correlation between these aforementioned mechanisms and LLJ frequency and intensity accounts for a large portion of the explained variance in precipitation. LLJ frequency and intensity, measured by 850 hPa wind speed, have been shown to be influenced by the El Niño Southern Oscillation (ENSO) and Pacific-North American teleconnection (e.g., Krishnamurthy et al. 2015; Liang et al. 2015; Danco and Martin 2018; Malloy and Kirtman 2020), Pacific and Atlantic SST anomalies and the North Atlantic Oscillation (NAO; e.g., Weaver and Nigam 2008; Weaver et al. 2009; Yu et al. 2015), as well as the CGT (e.g., Wang et al. 2013; Yu et al. 2015).

Seasonal drought and pluvial event evolution on the Great Plains is affected directly by LLJ associated precipitation and indirectly by both LLJ precipitation and frequency via their effect on regional precipitation recycling (e.g., Beljaars et al. 1996; Dirmeyer and Brubaker 1999; Schubert et al. 2004; Dirmeyer and Kinter III 2009; Basara et al. 2013). Consequently, LLJ and precipitation predictability are tightly linked.

Recent studies have established that LLJ moisture transport, vertical wind shear, and precipitation all significantly vary between jets that are strongly vs. weakly dynamically coupled to the upper-level jet stream (Burrows et al. 2019, 2020). Coupled LLJs, associated with upstream troughs (i.e., cyclonic wave activity) and greater atmospheric instability, are more intense and result in greater precipitation accumulations than uncoupled LLJs that occur with a ridge aloft (i.e., anticyclonic wave activity) and relatively less upper-level forcing (e.g., Burrows et al. 2019, 2020). It may also be observed that the change in sign of the correlation between central tropical Pacific SST and LLJ frequency from negative in April-May to positive in June-September (e.g., Krishnamurthy et al. 2015; Danco and Martin 2018), coincides with a shift in most likely LLJ class from coupled in May to uncoupled in June (Burrows et al. 2019, their Fig. 7). Taken together, these new findings beg the question: What new insights into Great Plains LLJ and precipitation predictability sources can be gained, if we partition the analyses by LLJ dynamical class?

This study presents the first detailed investigation of May 1901-2010 LLJ interannual variability in the context of LLJ dynamical coupling. The primary objective of the study is to bring to light robust teleconnections that govern May coupled and uncoupled Great Plains LLJ frequencies, and therefore, provide a new perspective on the predictability of LLJ-related precipitation in the Great Plains. The central Great Plains receives its maximum rainfall in May and during this period is a net sink for atmospheric moisture (Wang and Chen 2009). May soil moisture estimates are of great value to agriculture because they inform farmers about mean soil moisture state at the start of the growing season, as well as when planting is feasible. Previous studies have linked May soil moisture to subsequent summer precipitation (e.g., Meng and Quiring 2010). Ferguson and Wood (2011) showed a climatological tendency for local convection over wet soils, or regional precipitation recycling, in the Great Plains. Similarly, Cattiaux and Yiou (2013) demonstrated the contribution of the May precipitation deficit to the intensity of the ensuing summer drought in 2012.

The benefit of investigating teleconnection influence and seasonal forecast potential for LLJ class frequencies is that these more generic forecasts can likely be more skillful than those of precipitation and temperature themselves (e.g., Lavers et al. 2009; van den Hurk et al. 2012). Whereas previous studies tended to focus on June-August, focus is placed on May here because LLJs in this month tend to be more exposed to mid latitude teleconnections through the upper-level jet stream before the jet stream shifts poleward with the onset of summer and development of a ridge over the southern Great Plains. If frequencies of coupled and uncoupled LLJs and the positioning of their associated moisture convergence zones could be forecasted with any lead time, it would provide valuable information to the region's water resource managers and decision makers.

In this work, we apply LLJ detection and dynamical LLJ classification algorithms to the new CERA-20C (European Centre for Medium-Range Weather Forecast's 20^{th}-century coupled climate reanalysis; Laloyaux et al. 2018) 10-member/110-year (1901-2010) reanalysis in order to analyze the interannual to decadal scale variability of May uncoupled and coupled LLJs and teleconnections that govern their variability. Through detailed analyses of each jet class separately, and jointly in the context of atmospheric, Pacific, and Atlantic teleconnections, we are able to offer a novel perspective on each jet class's variability and potential predictability. Section 2 summarizes the data, spectral analysis method, LLJ detection and classification methods, and climate indices applied. Section 3 presents results on LLJ variability, major teleconnection influences, and a dynamical explanation of LLJ class variability; followed by summary and discussion in Section 4.

2. Data and Methodology

a. CERA-20C

The CERA-20C 10-member ensemble reanalysis is produced using the Integrated Forecast System version CY41R2, which comprises coupled atmospheric, land, ocean, wave, and sea ice model components. Its SSTs are nudged toward the monthly HadISST2 product (Titchner and Rayner 2014) to reduce model errors and yet allow for coupled process feedbacks. CERA-20C's slab ocean model assimilates observed sub-surface temperature and salinity profiles from the Met Office Hadley Centre EN4.0.2 data set (Good et al. 2013). CERA-20C assimilates quality controlled surface pressure and marine wind observations from the International Surface Pressure Databank (ISPDv3.2.6; Cram et al. 2015) and International Comprehensive Ocean-Atmosphere Data Set (ICOADSv2.5.1; Woodruff et al. 2011). CERA-20C incorporates CMIP5 atmospheric forcing data (i.e., solar forcing, greenhouse gases, ozone, and aerosols) to better capture 20^{th} century climate trends. Upper air (i.e., radiosonde) and modern-era satellite observations (post-1979) are not assimilated into CERA-20C to avoid spurious artificial trends that can be introduced due to changes in the underlying observational network (Thorne and Vose 2010). The land, wave, and sea-ice components do not assimilate any observations but are constrained by the dynamical coupling of the models.

CERA-20C has a spatial resolution of 125 km in the horizontal and 91 levels in the vertical dimension, from the surface to the 0.01 hPa level. All CERA-20C fields are available at 3-hourly temporal resolution. In this work, we have used the following CERA-20C 10-member ensemble mean fields: 0600 UTC 250 hPa, 500 hPa, and 850 hPa geopotential heights (Z250, Z500, and Z850), 0600 UTC 250 hPa, 700 hPa, and 850 hPa meridional winds (V250, V700, and V850); daily mean 2 m air temperature (T-2m), sea level pressure (SLP), and SST; and 1800 UTC (Day 0) to 1759 UTC (Day 1) accumulated precipitation. Wherever monthly means are presented, they are the means of these fields. For all climate indices, 1901-2010 is used to compute the climate normal unless otherwise specified.

Parallel analyses are conducted on the 80-member ensemble mean of the more recently released NOAA-CIRES-DOE 20^{th} Century Reanalysis version 3 (CRv3; Slivinski et al. 2019; Compo et al. 2011). CRv3 is available for a relatively longer time period of 1836-2015, at a global 1° x 1° spatial resolution, with 28 vertical pressure levels, and 3-hourly temporal resolution. In order to streamline the presentation of findings, CRv3 results are only mentioned selectively, when doing so benefits the discussion of CERA-20C based findings.

b. Multichannel Singular Spectrum Analysis

The interannual variability in low-level meridional winds over the continental U.S. is analyzed using a spectral technique called Multichannel Singular Spectrum Analysis (MSSA; Ghil et al. 2002), which is an extension of EOF analysis. MSSA gives the spatial and temporal structure of the oscillatory modes in a time-varying gridded dataset. Previously, MSSA has been used to identify the periodicity of oscillations in zonal winds, geopotential height, SSTs, and precipitation data (e.g., Plaut and Vautard 1994; Keenlyside et al. 2007; Krishnamurthy and Misra 2010; Karmakar et al.

2017; Agrawal et al. 2019). In this work, MSSA is used to identify significant oscillatory modes in monthly V850 anomalies for April-September during the 1901-2010 period, over the region from 20°-60° N, 150°-40° W (3528 grids). Monthly V850 anomalies are calculated by subtracting the 110-year mean and detrending the time series at each grid over the region. This V850 anomaly data consists of multiple time series (each of the same length N; N = 110 years) on a grid or map, where each grid within the domain constitutes one channel for the MSSA algorithm. A preliminary principal component analysis is performed on this data to reduce the number of channels from 3528 (total grids) to 50 and consequently, the computational time. These 50 channels explain more than 95% of the monthly V850 variance. MSSA is then applied to this extracted data of dimension 110×50 for each month (April-September) separately, using a window length of 8-years, which is suitable to resolve timescales between 2-8 years (Plaut and Vautard 1994). Note, window lengths between 5-8 years yielded similar estimates of 2-6 year time scale variances in May V850: the first four significant modes of oscillations are centered at the 3-4 year time period, with similar variances.

MSSA output consists of space-time EOFs and principal components that describe the spatial structure and periodicity of the oscillatory modes in V850. A significance test of the eigenmodes against 1000 red noise surrogates was carried out to identify statistically significant oscillatory modes (e.g., Allen and Robertson 1996; Ghil et al. 2002). The reconstructed 2-6 year variability mode is obtained by convolving all the significant space-time EOFs with corresponding space-time principal components, that have periodicity between 2-6 years, and then adding them together. The original data (V850) and the reconstructed data (2-6 year variability mode) both have the same length and units. A detailed discussion about MSSA can be found in Karmakar et al. (2017) and the references therein.

c. LLJ detection and classification

The Great Plains LLJ intensity peaks around midnight (0600-0900 UTC; e.g., Parish 2017; Burrows et al. 2019), with maximum wind speeds at approximately 850 hPa and a strong shear profile in the vertical direction up to 700 hPa (e.g., Bonner 1968; Whiteman et al. 1997). Based in part on the prior LLJ detection frameworks of Montini et al. (2019) and Tang et al. (2016), the 75^{th} percentiles of 1901-2010 May 0600 UTC V850 and V850-V700 wind shear are applied in LLJ detection. Specifically, a day is classified as a LLJ day if the 0600 UTC V850 and V850-V700 shear both exceed their respective 75^{th} percentiles at 10% or more of the ($1.25° \times 1.25°$) grids in the South Central Plains (SCP; 30°-42° N, 102°-92° W). The same method is applied to all warm-season months (i.e., April-September) using their respective 1901-2010 monthly climatological 75^{th} percentiles. The SCP region is used for detection because it encompasses the core of the climatological wind speed maximum associated with Great Plains LLJs.

Once detected, LLJ days are objectively classified into one of two dynamical classes– coupled and uncoupled– based on 0600 UTC 500 hPa local wave activity (LWA; Chen et al. 2015; Huang and Nakamura 2016). LWA quantifies the waviness in the meandering geopotential contours and can be expressed as the sum of cyclonic wave activity (CWA; trough) and anti-cyclonic wave (AWA; ridge) activity. LWA, CWA, and AWA are calculated from the 500 hPa geopotential height fields following the methodology of Burrows et al. (2019). Jet coupling in the SCP is evaluated on the basis of CWA in an upstream detection region located in the western U.S. (30°-42° N, 120°-102° W). In order for a LLJ day to be classified as a coupled LLJ (henceforth referred to as LLJC) at least one-third of the detection region's grids must have CWA values that exceed the region's 66^{th} percentile of grid-scale May 1901-2010

CWA. Otherwise, the LLJ day is classified as an uncoupled LLJ (henceforth referred to as LLJUC). LLJUC days are characterized by the presence of either a ridge over the SCP or a zonal upper-level circulation over the contiguous U.S. The 66^{th} percentile of CWA is chosen because it resulted in the best agreement between automated and visual map diagnosis of jet coupling in five randomly selected years. The CWA detection region is sized to match the meridional extent of SCP and cover the western U.S. region associated with substantial cyclonic wave activity in May. Burrows et al. (2019) applied a similarly positioned and sized CWA detection region.

The LLJ classification is not sensitive to small (±5°) zonal or meridional shifts in the placement of the CWA detection region, but is sensitive to changes in the CWA percentile threshold. For example, a change of ±5% in the CWA percentile threshold leads to a ~ 10% change in the number of LLJC. The higher the CWA percentile chosen for the detection threshold, the fewer jets that are classified as LLJC. The classification is equally well suited for April dynamical jet classification based on limited sample visual assessments. For June-September LLJs, however, users are encouraged to apply the two-pass approach of Burrows et al. (2019) that uses both local AWA and upstream CWA.

d. Composite analyses

We analyze the difference in mean meteorological fields between Mays with a higher number of LLJC(LLJUC) and Mays with a lower number of LLJC(LLJUC) in order to identify large scale circulation or teleconnection patterns that could explain these frequency differences. Mean composite differences are computed by subtracting the mean of lower quartile (0-25; Q1) LLJ frequency years from the mean of upper quartile (75-100; Q4) LLJ frequency years, based on the May frequency of LLJC (referred to as 'Q4-Q1 LLJC') and LLJUC (referred to as 'Q4-Q1

LLJUC'). Table 1 lists the years that constitute the upper and lower quartile years of LLJC and LLJUC; each quartile comprises 28 years. Significance of the composite differences are tested at the $\alpha = 0.1$ level using 10,000 bootstrapped samples. In order for a grid point difference to be significant, the bootstrapped 5-95 percentile range must not include zero.

e. Climate indices

1) Circumglobal Teleconnection Index

The CGT (Branstator 2002; Ding and Wang 2005) is a planetary-scale zonally-oriented Rossby wave pattern with a wavenumber five that manifests as geopotential anomalies guided by the upper-level jet stream. Ding and Wang (2005) concluded that CGT pattern variability is most strongly related to western Asia geopotential anomalies. Following them, we calculate a one-point correlation map for the 1901-2010 period between the May western Asia area-averaged Z250 (defined as R1; 35°-45° N, 60°-70° E) and the May Z250 at each grid point in the northern hemisphere (20°-80° N, 0°-360° E), to identify regions of strong covaribility with western Asia. Based on the correlation map (Fig. S1 b), three regions, or centers, that co-vary strongly with western Asia are identified: R2: 42°-52° N, 110°-120° E; R3: 32°-42° N, 155°-145° W; and R4: 33°-43° N, 118°-108° W. R3 varies in phase with the western Asia ridge (R1), whereas R2 and R4 are out of phase with R1 and are associated with troughs.

The May CGT index time series used in this study is calculated by subtracting the sum of R2 and R4 anomalies from the sum of R1 and R3 anomalies and normalizing the difference by the standard deviation of 1901-2010 CGT. This 4-center definition of CGT represents the hemisphere-scale variability well, especially over the North American sector. We examined the sensitivity of the May CGT index to the number of centers included (Fig. S1 b; marked with dashed boxes) and all derived CGT time series were fairly well correlated. An important point to note here is that R4 (33°-43° N, 118°-108° W) of our CGT index partially overlaps with the CWA detection region used in LLJ classification (Section 2.c). The correlation between area-averaged CWA over the CWA detection region and CGT is nearly 0.6, which is similar to the CGT index's correlation with R1-R4 Z250 anomalies.

2) Pacific Ocean indices

The Pacific Decadal Oscillation (PDO; Mantua and Hare 2002) index is calculated from the 1901-2010 monthly mean SSTs following the approach of Deser and Trenberth (2016). The SST anomalies are calculated by first removing the long-term annual cycle from monthly data, detrending SSTs at each grid, and subtracting global mean SST at each time step. The leading EOF pattern of the square root of the cosine of latitude-weighted SST anomalies over the North Pacific Ocean (20°-70° N, 110°-260° E) gives the PDO pattern and the first principal component, normalized by its standard deviation, gives the PDO index.

Oceanic Niño indices are used to study the ENSO (Trenberth 1997). The Niño3.4 index is calculated from the detrended SST anomalies over the Niño 3.4 region (5° S- 5° N, 170°-120° W), whereas the Niño 4 index is calculated similarly over the Niño 4 region (5° S- 5° N, 160° E-150° W). Both indices are computed for January-February-March (JFM) and May.

3) North Atlantic climate indices

The monthly NAO index (Hurrell 1995) is derived through an EOF analysis of monthly SLP over the Atlantic Ocean region between 20°- 80° N and 90°- 40° W following Hurrell et al. (2003). The leading EOF gives the NAO oscillation pattern, whereas the standardized principal component time series gives the NAO index. The North Atlantic Subtropical High index (NASH) is derived from May Z850 anomalies over the region covering 20°- 40° N and 60°- 30° W following Wei et al. (2019). The May NAO and NASH indices computed here have a 1901-2010 Pearson's correlation of 0.69 which is significant at the $\alpha = 0.1$ level. The Atlantic Multi-Decadal Oscillation index (AMO; Trenberth and Shea 2006) is calculated from annual mean SSTs over the Atlantic basin (0°- 60° N, 80° W- 0° E) from 1901-2010. SST anomalies are calculated by subtracting the 1901-1970 climatological means at each grid point and then area-averaging over the Atlantic basin. Finally, this time series is detrended by subtracting the global mean SST anomaly time series. For all correlation analyses between climate indices and the LLJC or LLJUC frequency time series, correlation significance is tested at the $\alpha = 0.1$ level using the bootstrapping method with 10,000 realizations of the 110 year time series. The correlation between two time series is significant at the $\alpha = 0.1$ level if the 5-95 percentile range of 10,000 bootstrapped correlations does not include zero.

3. Results

a. Warm-Season LLJ Statistics

An MSSA (Section 2.b) of CERA-20C′s April-September monthly mean 0600 UTC V850 for the 1901-2010 period reveals substantial variability over the Great Plains with 2-6 year periodicity. Figure 1a illustrates the total interannual standard deviation and the standard deviation of the filtered 2-6 year oscillatory mode of April-September monthly mean 0600 UTC V850 over the SCP. The results for May are particularly noteworthy given the socioeconomic importance of May precipitation predictability and the relative lack of studies focused on May, as discussed in the Introduction. May has the strongest interannual variation of V850 among warm season months, with nearly 38% of the total interannual variability explained by the 2-6 year oscillatory mode, suggesting a plausible large scale atmospheric teleconnection influence. Figure 1b shows the contribution of each month's LLJ count and precipitation accumulation to warm season totals. May comprises 15% of all warm season LLJs but nearly 25% of the warm season total precipitation. Spatially, the climatological LLJ core (i.e., maximum V850) and the maximum in the standard deviation of the May V850 filtered 2-6 year oscillatory mode lie over the SCP (Fig. 1c). Nearly all LLJs traverse the SCP regardless of where they eventually end (e.g., Burrows et al. 2019). Thus, the selection of this region for further detailed analyses makes sense from both prediction and statistical robustness perspectives.

Figure 2a presents the May SCP LLJT (total LLJs), LLJC, and LLJUC frequency time series, showing their year-to-year variability. For the 1901-2010 period, 1626 May LLJT events are identified, out of which 831 are LLJC and 795 are LLJUC. Similar calculations applied to the CRv3 dataset produced 1673 LLJT, 779 LLJC, and 894 LLJUC in May for the 1901-2010 period. May has an average of 15 LLJ days, with an almost 50-50 ratio of LLJC and LLJUC, similar to that reported by Burrows et al. (2019). Time series analysis reveals an inverse relationship between LLJC and LLJUC frequencies (Pearson's $r = -0.5$, significant at the $\alpha = 0.1$ level).

It can be noted from Fig. 2b that though the frequencies of LLJC and LLJUC are very similar in May (almost 50-50 ratio), LLJCs are associated with stronger V850 and more precipitation over the SCP. Mean differences between LLJC and LLJUC event V850 is 3.44 m s^{-1} and associated precipitation is 1.35 mm d^{-1}, and these differences are significant at the $\alpha = 0.1$ level. Overall, nearly 41% of May SCP precipitation is associated with LLJ events, out of which 62% is received on LLJC days and 38% is received on LLJUC days. May monthly averaged SCP precipitation has a weak positive correlation with LLJC frequency ($r = 0.16$) and a strong negative correlation with LLJUC frequency ($r = -0.46$). A significantly more positive precipitation–LLJC frequency correlation ($r = 0.47$) is found if we compare SCP LLJC frequency with precipitation in the region offset just 10° north (i.e., 102°-92° W, 40°-52° N), consistent with typical LLJ exit and moisture convergence positioning (e.g., Ferguson et al. 2020). These statistics underscore how variations in frequencies of LLJC and LLJUC can impact the hydroclimate of the region.

The spatial patterns of May Q4-Q1 LLJC and Q4-Q1 LLJUC precipitation composites (Fig. 3) show significant differences in precipitation across the globe during high and low LLJC and LLJUC frequency years. Notable precipitation differences exist not only over the SCP and Midwest U.S., but also over the Intra-Americas Sea, the tropical and northeastern Pacific Ocean, Southeast Asia, and the Indian Ocean; implying large scale remote influences on Great Plains LLJs. Henceforth, we analyze the LLJC and LLJUC time series separately and pursue attribution of their respective interannual frequency variations to large scale teleconnection patterns.

b. LLJC and LLJUC Synoptic Overview

Figure 4 shows the Q4-Q1 LLJC and Q4-Q1 LLJUC composites of May 0600 UTC Z500 and Z250. The CGT wavenumber five pattern is distinctly seen over the Northern Hemisphere in the Q4-Q1 LLJC composite. Significant positive Z500 anomalies can be noted in the following regions: western Asia, the northwestern Pacific Ocean, the northeastern Pacific Ocean, eastern North America, and Greenland. Significant negative Z500 anomalies can be seen in the following regions: eastern China, the Aleutian Islands, the western U.S., and the north-central Atlantic Ocean. The Z500 anomaly pattern is closely matched by that of the Z250 anomalies (Fig. 4a), indicative of the barotropic structure of the centers of action of the CGT, with the only exception being the western Asia ridge that has a heat-low type circulation near the surface (Ding and Wang 2005).

The Q4-Q1 LLJUC composite (Fig. 4b) features a combination of a wavenumber four and wavenumber two pattern, with significantly positive Z500 and Z250 anomalies over eastern Asia, the Aleutian Islands, the contiguous U.S., and the northern Atlantic Ocean and a significantly negative anomaly center in western Asia. The wave-like pattern in Q4-Q1 composites is more clear in some of the individual CERA-20C ensemble members, such as the first member as shown in Fig. S3. The scale of the positive anomaly centers in Q4-Q1 LLJUC is different as compared to the LLJC composite and they appear more zonal in case of LLJUC. Additionally, the pronounced meridional Z250 gradient over north America (Fig. 4b) is consistent with a stronger zonally oriented upper level jet between 40°-60° N (Fig. S4). A poleward-shifted jet favors more persistent ridges over the CONUS, a condition more favorable for LLJUCs as compared to LLJCs. Possible interference from other teleconnections is also examined in a later section. The Q4-Q1 LLJT composite of May Z500/Z250 does not reveal a clear CGT-like wave pattern (Fig. 4c), which could explain why CGT-LLJ connections have been overlooked in the literature. A strong CGT influence only becomes apparent when the two classes of LLJs are analyzed separately.

Near the surface, May T-2m anomalies for Q4-Q1 LLJC and LLJUC composites are generally in agreement with the geopotential anomalies aloft (Fig. 5a-b). T-2m anomalies are much larger over continental longitudes as compared to oceanic longitudes, likely due to lower heat capacity of the land surface as compared to the ocean. In the Q4-Q1 LLJC composite, significant heating anomalies exist over western Asia and the eastern U.S., whereas significant heating anomalies exist over northeastern China centered near 40° N, 105° E and western North America centered near 35° N, 110° W in the Q4-Q1 LLJUC composite. These T-2m anomaly patterns influence the May west-east surface temperature gradient over the U.S., which in turn can modulate LLJC and LLJUC intensity and frequencies (e.g., Holton 1967). The Hovmöller plots of Fig. 5c-d illustrate the eastward propagation of T-2m anomalies from 1 March to 31 May attributable to upper-level circulation anomalies (Fig. 4). Heating anomalies– especially over elevated land such as the Rockies– can also result in phase-locking with the propagating Rossby wave and thus help in establishing a particular phase of quasi-stationary Rossby wave over the midlatitudes (e.g., Koster et al. 2016; Wang et al. 2019).

c. LLJC and LLJUC Teleconnections

1) The Circumglobal Teleconnection

The CGT has previously been associated with the summer precipitation variability over the U.S. (e.g., Ding and Wang 2005; Wang et al. 2010b; Ding et al. 2011), but its direct influence on LLJ dynamical coupling (i.e., LLJC vs. LLJUC) has not been investigated in detail before. The time series of the May CGT index (Section 2.e.1) illustrated in Fig. 6a shows considerable interannual variability. Like Great Plains LLJs, May CGT has considerable variability at 2-6 year time scales (Figs. 2 & 6a). The CGT power spectrum peaks near 3-, 4- and 6-year periodicity exceed the 90% bound of the red noise power spectrum (Fig. 6b). A regression of May CGT with May Z250 shows the positive phase of the CGT (Fig. 6c), which can also be clearly seen in Q4-Q1 LLJC composites of Z250, Z500, and T-2m (Fig. 4a and Fig. 5a).

From a time series analysis, it is found that May CGT explains nearly one-third of the interannual variability of May LLJC and LLJUC frequencies. May CGT is strongly correlated with May LLJC frequency for the 1901-2010 period, $r = 0.62$, which explains nearly 38% of the interannual variance in LLJC frequency. The correlation between May CGT and May LLJUC frequency is -0.48, explaining nearly 23% of LLJUC frequency interannual variance. These correlations between CGT and the LLJC and LLJUC frequency timeseries are significant at the $\alpha = 0.1$ level. An important observation here is that the strength of the negative CGT-LLJUC correlation is weaker as compared to the positive CGT-LLJC correlation, which explains why the negative CGT phase is not distinct in the Q4-Q1 LLJUC Z500 composites (Fig. 4b). The correlation between May CGT and LLJT frequency is just 0.15, which again underscores the need to study the two classes of LLJs separately (Table 2). Similar but slightly weaker correlations between CGT and LLJs are found using the CRv3 dataset for the 1901-2010 period; correlations between CGT and LLJT, LLJC, and LLJUC are 0.11, 0.49, and -0.31, respectively.

2) Pacific and Atlantic Teleconnections

(i) Pacific Ocean Teleconnections: To take a closer look at the influence of SST variability on May LLJC and LLJUC frequencies, SST composite anomalies for May and the previous winter (JFM) based on Q4-Q1 composites of May LLJC and LLJUC are constructed (Fig. 7). For the May Q4-Q1 LLJC composite, we notice a negative PDO phase (i.e., horseshoe pattern in the northern Pacific Ocean) and negative SST anomalies over the equatorial Pacific Ocean (i.e., the Niño3.4 region), which shows in-phase variability of PDO and ENSO (Fig. 7a). Strong negative SST anomalies off the western U.S. coast imply a higher frequency of trough passages over the western U.S., also evident in Fig. 4a, that support a greater frequency of LLJCs over the SCP. By comparison, in the May Q4-Q1 LLJUC composite, features of a positive PDO phase are noticeable over the North Pacific, but not over the equatorial Pacific (Fig. 7b). Again, strong positive SST anomalies off the western U.S. coast imply a more poleward-shifted jet stream, a higher frequency of ridge building over the western U.S. extending to the SCP (also

seen in Fig. 4b), and consequently, a higher frequency of LLJUCs over the SCP. SST Q4-Q1 LLJC and LLJUC composites have PDO and ENSO phases in JFM that are similar to their respective phases in May, implying some influence from previous winter SST anomalies (Fig. 7c-d).

Table 2B summarizes the Pearson correlation coefficients and r^2 values between May LLJ frequencies (LLJT, LLJC, and LLJUC) and several SST-based climate indices. Note that here no temporal smoothing is performed on the May PDO index before computing correlations with LLJ frequencies to quantify PDO-LLJ teleconnections at interannual time scale. The May PDO index and LLJC frequency are significantly negatively correlated ($r = -0.22$), but PDO explains only 5% of the variance in May LLJC frequency. May LLJUC frequency and JFM Niño 3.4 and Niño 4 indices have significant negative correlations ($r = -0.17$). This negative correlation could be partly related to La Niña associated winter warm surface temperature anomalies over the western U.S. that could persist through May (e.g., Ropelewski and Halpert 1986; Wang and Schubert 2014, Fig. S5 a-b). In addition, significant negative correlation values are also found between May LLJT frequency and May and JFM Niño 3.4 and Niño 4 indices (r -0.22). The negative correlation between May LLJT and ENSO seen here is consistent with previous studies that have shown ENSO modulates spring-time Great Plains LLJ frequency through sea level pressure variations in the Gulf of Mexico (e.g., Liang et al. 2015; Krishnamurthy et al. 2015).

(ii) North Atlantic Teleconnections: Significant SST anomalies are noted in the North Altantic Ocean in the SST Q4-Q1 composites of May LLJC and LLJUC (Fig. 7). Three indices— NAO, NASH, and AMO— that capture North Atlantic climate variability are examined for co-variability with May LLJC and LLJUC frequencies (Table 2C). We found a significant positive correlation between May NAO and LLJUC frequency ($r = 0.33$), and also between May NASH and LLJUC

frequency ($r = 0.23$), which is expected because NAO and NASH are strongly correlated ($r = 0.69$). Figure 8 shows the regression slope between May NAO and May Z500. These Z500 regression coefficients imply a poleward-shifted jet stream over North America and the North Atlantic (Fig. S5 c), and persistent ridge-like circulation over the southwestern U.S. and Great Plains, favoring higher LLJUC frequency. This pattern explains the zonal elongation of Z500 anomalies in the case of Q4-Q1 LLJUC (Fig. 4b). LLJC frequency is not found to have any significant Atlantic Ocean influence in May. We speculate that since NASH is very weak in May as compared to its summer climatology (Fig. 8b), the NASH western ridge-Great Plain LLJ connection (e.g., Wei et al. 2019) is similarly weak or nonexistent. NASH is correlated with LLJUC frequency only due to its strong correlation with NAO. Similarly, AMO is uncorrelated with May LLJC and LLJUC frequencies; because AMO exerts its influence on Great Plain LLJs in the summer months mainly via modulation of NASH (e.g., Hu et al. 2011; Oglesby et al. 2012). It can be concluded from here that the direct contribution from Pacific and North Atlantic climate variability is rather small as compared to the CGT's contribution to interannual variability of May SCP LLJCs and LLJUC frequencies.

d. Decadal variability in CGT-LLJ Teleconnection

Having established that a strong, significant correlation exists between May CGT and LLJC and LLJUC frequencies, we examine low-frequency variability in these correlations during the 20^{th} century. Figure 9a (b) shows the 21-year running window correlations between May CGT and LLJC (LLJUC) frequency and their 90% confidence intervals. Superimposed on these plots is the 10-year running mean of the May PDO index. PDO was mostly negative during 1905-1924, 1945-1977, and 2003-2010 and mostly positive during 1925-1944 and 1978-2002. The highs and lows in 21-year CGT-LLJUC correlations tend to vary in synchronization with PDO's decadal scale variability; CGT-LLJUC 21-year correlations are higher during the positive PDO phase (i.e., approx. 1934-36, 1981-86) and lower during the negative PDO phase (i.e., approx. 1951-53, 1964-66). The 21-year CGT-LLJC correlations also exhibit decadal scale variability; correlations are significantly lower for some years during the positive PDO phase (i.e., approx. 1925-29) and higher for other years during the negative PDO phase (i.e., approx. 1959-63; Table 2A). Results obtained from a parallel analysis using CRv3 data are very similar and thus lend greater confidence to the CGT-LLJ teleconnection results and their PDO-like decadal variability shown here for CERA20C– especially for the latter part of the 20^{th} century (Figs. S6, S7). A brief analysis of the PDO-related variability follows.

Figure 9c illustrates the mean LLJC and LLJUC frequencies during positive (N = 54) and negative (N = 56) PDO years (shown with solid circles). The 90% confidence intervals on the mean values are calculated from 10,000 bootstrapped samples of 54 years by selecting 25 years with replacement each time. Although LLJC and LLJUC frequencies vary with PDO phase, the differences are not statistically significant. An important significant difference is a higher LLJUC frequency in the positive PDO years as compared to LLJC frequency.

Next, we use four 25-year subsets conditioned on joint CGT and PDO phases (i.e., $+CGT|+PDO$, $+CGT|-PDO$, $-CGT|+PDO$, and $-CGT|-PDO$; years are listed in Table S1) to examine the changes in LLJC and LLJUC frequencies in accordance with CGT and PDO phases. By applying the same bootstrapping method on samples of 25 years, LLJC and LLJUC confidence intervals are computed for all four CGT/PDO conditional subsets. It can be noted from Fig. 9c that positive CGT years (shown with open circles) have a significantly higher frequency of LLJCs as compared to negative CGT years (shown with open squares) and conversely, negative CGT years have a significantly higher frequency of LLJUCs as compared to positive CGT years. However, modulation of these frequencies by PDO is not statistically significant at the $\alpha = 0.1$ level during positive or negative CGT years.

Recent studies have pointed out that PDO is not a single phenomenon, but rather the integrated effect of multiple processes such as: tropical Pacific SST and precipitation variability, SST anomalies near Kuroshio and Oyashio frontal zones, Aleutian low fluctuations, internal atmospheric variability, etc. (see Newman et al. (2016) and references therein). Precipitation anomalies related to the tropical Indo-Pacific Ocean SST anomalies are also recognized as one major forcing of low-frequency PDO variability (e.g., Deser et al. 2004). Thus, any PDO-like decadal variability could be the combined result of processes that influence North Pacific SSTs at decadal time scales, and not actually caused by local North Pacific SST anomalies. PDO-related SST anomalies can still have a small indirect influence on the atmospheric circulations aloft via the Kuroshio-Oyashio region's SST anomalies and Western Pacific Subtropical High (WPSH) mostly in summer (e.g., Matsumura and Horinouchi 2016).

May precipitation and Z250 differences between PDO phases are examined to find a potential source of decadal variability. We note significant differences in May precipitation over the western tropical Pacific (Fig. 10a) and associated changes in the May Z250 fields, with a significant increase in Z250 over the WPSH region and the adjoining western U.S. region during positive PDO years (Fig. 10b). Another region with significant PDO-related precipitation differences is the Kuroshio region, possibly related to Z250 anomalies over northeastern Asia. Figures 11a-b and d-e show the May Z250 anomalies for the four subsets of CGT/PDO conditional years analyzed in Fig. 9c. May Z250 anomalies are computed by subtracting the 110-year mean May Z250 at each grid. The Z250 anomalies show some variations in the magnitude of troughs and ridges of the Rossby wave during both positive and negative CGT years. Significant differences are seen in eastern Asia, the western U.S., and northeastern America between PDO phases in Fig. 11c,f. We speculate that variations in CGT during PDO phases could be related to PDO associated precipitation and Z250 anomalies seen in Fig. 10.

During a positive PDO phase, positive Z250 anomalies over the western U.S., tend to significantly strengthen ridge building there (i.e., CGT center R4) and supports a higher frequency of LLJUCs as compared to LLJCs (Fig. 10b). Further investigation of PDO-CGT physical linkages and mechanistic pathways through which LLJC and LLJUC frequencies are impacted would require idealized modeling simulations (e.g., with prescribed SSTs over the North Pacific, diabatic heating anomalies over the western-central Pacific, etc.) that extends beyond the focus and scope of the current work.

e. Dynamics of LLJC and LLJUC Variability

Finally, we present a dynamical explanation of LLJ jet class variability over the contiguous U.S. that is linked to the observed CGT-LLJC(LLJUC) teleconnection. The impact of CGT on LLJ jet class can be mainly explained using mechanisms offered by Parish (2017) and Holton (1967). We focus on the changes in Z850, T-2m, and V850 over the region spanning 120°-70° W and 30°-42° N between year subsets conditioned jointly on CGT and PDO phase (Table S1). Figure 12a illustrates the May Z850 east-west gradients over the SCP latitudinal extent for positive CGT (blue lines) and negative CGT (red lines) years. A sharp east-west gradient in Z850 in both positive CGT and negative CGT composites is the result of differential heating over the sloping terrains of Great Plains due to solar insolation in summer and constitutes the region's background southerly geostrophic flow (e.g., Parish 2017). The Z850 gradient is enhanced by a positive CGT and suppressed by a negative CGT (Fig. 12a). Additionally, a dynamically-driven 850 hPa lee trough can develop to the east of the Rockies in response to an upstream upper-level trough, more likely with the positive CGT phase, and enhance the Z850 east-west gradient.

Similarly, near surface temperatures are also modulated by CGT phase. Figure 12b illustrates the May T-2m anomalies from west to east and a clear distinction can be made between positive CGT and negative CGT years. The negative T-2m anomalies in the west and positive T-2m anomalies in the east in the case of positive CGT, are consistent with a potential enhancement of the nocturnal southerly LLJ via thermal wind forcing in lower levels (e.g., Holton 1967). During positive CGT years, a negative PDO phase is associated with a stronger east-west T-2m gradient (see Fig. S8 for regions with significant differences in T-2m). During negative CGT years, the T-2m anomalies in the western U.S. are significantly higher during the positive PDO phase as compared to the negative PDO phase, related to more persistent ridges over the western U.S. during the positive PDO phase (Fig. 11f).

Relatedly, mean May 0600 UTC V850 between 100°-80° W is significantly higher during positive CGT years as compared to negative CGT years (Fig. 12c) due to stronger background geostrophic flow and supporting T-2m anomalies (Fig. 12a,b). The ageostrophic wind component, supported by nocturnal decoupling of the boundary layer (e.g., Blackadar 1957), shows much smaller differences between CGT phases as compared to the geostrophic wind component (Fig. S9). Recall here that positive and negative CGT phases favor LLJC and LLJUC frequencies, respectively (Table 2A), and also that LLJCs have significantly stronger meridional winds as compared to LLJUCs (Fig. 2). Modulation of monthly mean May V850 by PDO phase is not significant during positive or negative CGT years. But as shown next (Fig. 12d), V850 differences between positive and negative PDO phases are significant during positive CGT years if only May LLJC days are considered.

Figures 12d-e show the spatial pattern of V850 anomalies on LLJC and LLJUC days computed by averaging over only the LLJC or LLJUC days in May as opposed to all the days in May (Figs. 12a-c). For LLJC days, SCP V850 is significantly lower in $+CGT|+PDO$ years as compared to $+CGT|-PDO$ years (Fig. 12d). On the contrary, for LLJUC days, no significant SCP V850 differences are noted between $-CGT|+PDO$ and $-CGT|-PDO$ year composites. Given that LLJUCs are associated with ridge-like circulation aloft that impose similar Z850 and T-2m gradients over the Great Plains regardless of PDO phase, this finding is not surprising (Fig. 12a-b).

Large differences in Z850 and T-2m over the western U.S. (R4 center in the CGT index) between CGT and PDO phases (Figs. 12a-b) motivated us to examine the correlation structure between R4's Z250 anomalies with LLJC and LLJUC frequency time series. R4 May Z250 anomalies are computed by subtracting the 110-year mean May Z250. We found that the correlations between May R4 Z250 anomalies and May LLJC ($r = -0.74$) and LLJUC ($r = 0.58$) frequency time series exceeded the correlations between them and the May CGT time series. Correlations between LLJC and LLJUC frequency time series and Z250 at other CGT centers (i.e., R1-R3) was weaker than with R4 Z250. Given the geographic proximity of R4 to the Great Plains and established relationship between R4 geopotential anomalies and dynamical jet class, the strong correlation should not come as a surprise. From a lead forecast standpoint, it is important to evaluate the covariability of upstream CGT centers to R4. Table 3 summarizes the correlation between Z250 at all four CGT centers, considered in this analysis. R4's significant co-variability with R2 and R3 through the CGT offers some scope for LLJ predictability at a sub-monthly lead time. Whatever downstream contiguous U.S. predictability that will exist will occur with amplified North Pacific flow regimes relative to climatology when the Z250 anomalies in R2 and R3 are out of phase.

4. Summary and Discussion

Through spectral analysis of V850 from the 110-year CERA-20C reanalysis dataset, we show that over the SCP 1) the greatest warm season interannual variability in LLJ frequency occurs in May and 2) the V850 2-6 year variability mode contributes nearly 38% of the total variance. This is crucial because LLJs contribute 41% of May precipitation in the SCP, which amounts to 25% of the total April-September precipitation (Fig. 1). The prominence of LLJs′ 2-6 year variability mode points to a large scale teleconnection component to May LLJ variability, a connection which, to our knowledge, has not previously been explained dynamically.

In this study, by analyzing May SCP LLJC and LLJUC frequency time series separately over the century-scale record afforded by CERA-20C, we are able to successfully demonstrate a significant May CGT-LLJC(LLJUC) teleconnection. The split analyses of teleconnection influences on LLJC and LLJUC aid in identifying for the first time, a very clear signature of the CGT influence in May (Fig. 4). Positive and negative phases of CGT increased LLJC (CGT-LLJC: $r = 0.62$) and LLJUC (CGT-LLJUC: $r = -0.48$) event frequencies, respectively. It is found that May CGT explains 38% of variability in LLJC frequency and 23% of variability in LLJUC frequency (Table 2A). Like Great Plains LLJs, the CGT index also demonstrates considerable interannual variability with 2-6 year periodicity (Figs. 2 & Fig. 6). Besides the CGT, a significant but less substantial correlation is found between May NAO and LLJUC frequency ($r = 0.33$;

Fig. 8). Overall, Pacific and North Atlantic climate variability explain very little interannual variability in LLJC and LLJUC frequencies (Fig. 7; Table 2B-C).

The synoptic and dynamical linkages between the CGT and LLJC and LLJUC frequencies begins over the western U.S., where the upper-level ridge/trough pattern associated with the CGT strongly modulates background Z850 and near-surface temperature gradients setup by differential heating over the Rockies-Plains sloping terrain. The resultant geopotential and thermal gradients determine the geostrophic wind flow within the Great Plains LLJ corridor. Surface heating/cooling anomalies over the elevated terrain of the western U.S. (Fig. 5) can further support phase-locking of the CGT wave train over certain longitudes through feedback on upper-level circulation anomalies (e.g., Koster et al. 2016; Wang et al. 2019). Owing to this direct connection between the western U.S. and the Great Plains, a higher correlation is found between western U.S. May Z250 and May LLJC ($r = -0.74$) and LLJUC ($r = 0.58$) frequencies than between the CGT and LLJC or LLJUC frequencies. Nevertheless, significant correlations between western U.S. Z250 and upstream CGT centers of action underscore the importance of CGT and its potential role in LLJ predictability (Table 3). Prediction lead times will depend upon prediction skills for midlatitude atmospheric circulations (e.g., Teng et al. 2013).

Importantly, the CGT-LLJC and CGT-LLJUC relationships exhibit decadal scale variability in association with PDO phase (Fig. 9). PDO phase change significantly affects LLJC and LLJUC intensity and frequency respectively over the SCP (Figs. 12 and 9c), mainly through modulation of the CGT wave train (Fig. 11). Low-frequency PDO-like variability could be linked to multiple processes that affect North Pacific SSTs (Newman et al. 2016). We found significant precipitation anomalies in the western tropical Pacific and the Kuroshio region and associated changes in geopotential height over the western U.S. and northeastern between PDO phases (Fig. 10). PDO-related decadal scale changes in other teleconnections across the globe have been noted in previous studies (e.g., Watanabe and Yamazaki 2014; Chakraborty and Agrawal 2017; Cai et al. 2010; Wang et al. 2008). Given that previous studies have reported a significant trend in total springtime LLJs and precipitation over the SCP (e.g., Barandiaran et al. 2013; Cook et al. 2008), it is worth revisiting this work in light of the noted decadal variability in LLJC and LLJUC frequencies with PDO phase. The availability of century-long reanalysis datasets like CERA20C and CRv3 can be pivotal in these studies.

The CGT could also offer some explanation for the noted summer temperature and precipitation co-variability between Asia and North America (e.g., Li et al. 2005; Zhu and Li 2016). Interestingly, Indian monsoon onset exhibits similar sensitivity to May geopotential and surface temperature anomalies in western Asia (Agrawal 2018) as noted for May LLJC frequency (Fig. 5a), indicative of the CGT influence. During June-September, the CGT is influenced by both the Indian monsoon (e.g., Sardeshmukh and Hoskins 1988; Joseph and Srinivasan 1999; Ding and Wang 2005; Beverley et al. 2019) and the East Asian monsoon (e.g., Zhou et al. 2020) and can be sustained through convective heating anomalies over these monsoon regions. In our investigation of the CGT-LLJ teleconnection for shoulder spring months April and June, we found the April CGT pattern to be very weak and lacking a distinct wavenumber-five signature. The June CGT dipole pattern over North America was located at nearly 50° N and June CGT was significantly correlated with June SCP LLJT frequency ($r = 0.4$) (see Supplementary text, Figures S1-S2). Atlantic Ocean-related variability like NASH and AMO is another important consideration for June-September LLJ predictability (e.g., Cook et al. 2008; Li et al. 2012; Wei et al. 2019).

In closing, the results presented in this work are significant because they provide a starting point for potentially longer lead forecasts of LLJC and LLJUC frequencies, which are closely correlated with the Great Plains wind resources and hydroclimate (e.g., Burrows et al. 2019, 2020). Improving the predictability of LLJ class frequencies would provide critical information to water resources and agricultural planners in the region. A future modeling experiment will be conducted to quantify the contribution of local heating anomalies over western North America versus remote surface heating anomalies over Asia to the Great Plains LLJ class frequencies. The experiment will importantly build upon the analyses presented here and broaden the focus to April-September to additionally examine the role of the summer NASH in forcing LLJ class frequencies.

Acknowledgments. This work was funded by NSF award AGS-1638936. SA conceived the study, performed all analyses, and co-wrote the manuscript with CF. LB and CF contributed to the design of the study. All authors contributed to the discussions and interpretation of results.

Data availability statement. CERA-20C 10-member ensemble data was obtained from ECMWF via a dedicated data portal (`http://apps.ecmwf.int/datasets`). CRv3 80-member ensemble mean data was obtained from `https://psl.noaa.gov/data/gridded/data.20thC_ReanV3.pressure.html`. The low-level jet frequency time series and climate indices calculated for this study are available upon request.

References

Agrawal, S., 2018: Impact of local and remote land-atmosphere coupling on the indian summer monsoon. Ph.D. thesis, Indian Institute of Science.

Agrawal, S., A. Chakraborty, N. Karmakar, S. Moulds, A. Mijic, and W. Buytaert, 2019: Effects of winter and summer-time irrigation over gangetic plain on the mean and intraseasonal variability of indian summer monsoon. *Climate Dynamics*, **53 (5)**, 3147–3166, doi: 10.1007/s00382-019-04691-7.

Algarra, I., J. Eiras-Barca, G. Miguez-Macho, R. Nieto, and L. Gimeno, 2019: On the assessment of the moisture transport by the great plains low-level jet. *Earth System Dynamics*, **10 (1)**, 107–119, doi:10.5194/esd-10-107-2019, URL https://www.earth-syst-dynam.net/10/107/2019/.

Allen, M. R., and A. W. Robertson, 1996: Distinguishing modulated oscillations from coloured noise in multivariate datasets. *Climate Dynamics*, **12 (11)**, 775–784, doi:10.1007/s003820050142.

AWEA, 2018: Wind facts at a glance. American Wind Energy Association, https://www.awea.org/wind-101/basics-of-windenergy/wind-facts-at-a-glance.

Barandiaran, D., S.-Y. Wang, and K. Hilburn, 2013: Observed trends in the great plains low-level jet and associated precipitation changes in relation to recent droughts. *Geophysical Research Letters*, **40 (23)**, 6247–6251, doi:10.1002/2013GL058296.

Basara, J. B., J. N. Maybourn, C. M. Peirano, J. E. Tate, P. J. Brown, J. D. Hoey, and B. R. Smith, 2013: Drought and associated impacts in the great plains of the united states-a review. *International Journal of Geosciences*, **4 (6B)**, doi:10.4236/ijg.2013.46A2009.

Beljaars, A. C. M., P. Viterbo, M. J. Miller, and A. K. Betts, 1996: The anomalous rainfall over the united states during july 1993: Sensitivity to land surface parameterization and soil moisture anomalies. *Monthly Weather Review*, **124 (3)**, 362–383, doi:10.1175/1520-0493(1996)124<0362:TAROTU>2.0.CO;2.

Beverley, J. D., S. J. Woolnough, L. H. Baker, S. J. Johnson, and A. Weisheimer, 2019: The northern hemisphere circumglobal teleconnection in a seasonal forecast model and its relationship to european summer forecast skill. *Climate Dynamics*, **52 (5)**, 3759–3771, doi: 10.1007/s00382-018-4371-4.

Blackadar, A. K., 1957: Boundary Layer Wind Maxima and Their Significance for the Growth of Nocturnal Inversions. *Bulletin of the American Meteorological Society*, **38 (5)**, 283–290, doi:10.1175/1520-0477-38.5.283.

Bonner, W. D., 1968: Climatology of the low level jet. *Monthly Weather Review*, **96 (12)**, 833–850, doi:10.1175/1520-0493(1968)096<0833:COTLLJ>2.0.CO;2.

Branstator, G., 2002: Circumglobal teleconnections, the jet stream waveguide, and the north atlantic oscillation. *Journal of Climate*, **15 (14)**, 1893–1910, doi:10.1175/1520-0442(2002)015<1893:CTTJSW>2.0.CO;2.

Burrows, D. A., C. R. Ferguson, and L. F. Bosart, 2020: The role of upper-level coupling on Great Plains low-level jet structure and variability. *Journal of the Atmospheric Sciences*, 1–54, doi:10.1175/JAS-D-20-0059.1.

Burrows, D. A., C. R. Ferguson, M. A. Campbell, G. Xia, and L. F. Bosart, 2019: An objective classification and analysis of upper-level coupling to the great plains low-level jet over the twentieth century. *Journal of Climate*, **32 (21)**, 7127–7152, doi:10.1175/JCLI-D-18-0891.1.

Cai, W., P. Van Rensch, T. Cowan, and A. Sullivan, 2010: Asymmetry in enso teleconnection with regional rainfall, its multidecadal variability, and impact. *Journal of Climate*, **23 (18)**, 4944–4955.

Cattiaux, J., and P. Yiou, 2013: Ch. 4: U.s. heat waves of spring and summer 2012 from the flow-analogue perspective. *Explaining extreme events of 2012 from a climate perspective*, Bull. Am. Meteorol. Soc., 94(9), S1–S74.

Chakraborty, A., and S. Agrawal, 2017: Role of west asian surface pressure in summer monsoon onset over central india. *Environmental Research Letters*, **12 (7)**, 074 002, doi:https://doi.org/10.1088/1748-9326/aa76ca.

Chen, G., J. Lu, D. A. Burrows, and L.-Y. R. Leung, 2015: Local finite-amplitude wave activity as an objective diagnostic of midlatitude extreme weather. *Geophysical Research Letters*, **42 (24)**, doi:10.1002/2015GL066959.

Christian, J., K. Christian, and J. B. Basara, 2015: Drought and pluvial dipole events within the great plains of the united states. *Journal of Applied Meteorology and Climatology*, **54 (9)**, 1886–1898, doi:10.1175/JAMC-D-15-0002.1.

Compo, G. P., and Coauthors, 2011: The twentieth century reanalysis project. *Quarterly Journal of the Royal Meteorological Society*, **137 (654)**, 1–28, doi:10.1002/qj.776.

Cook, K. H., E. K. Vizy, Z. S. Launer, and C. M. Patricola, 2008: Springtime intensification of the great plains low-level jet and midwest precipitation in gcm simulations of the twenty-first century. *Journal of Climate*, **21 (23)**, 6321–6340, doi:10.1175/2008JCLI2355.1.

Cram, T. A., and Coauthors, 2015: The international surface pressure databank version 2. *Geoscience Data Journal*, **2 (1)**, 31–46, doi:10.1002/gdj3.25.

Dai, A., 2013: The influence of the inter-decadal pacific oscillation on us precipitation during 1923–2010. *Climate Dynamics*, **41 (3)**, 633–646, doi:10.1007/s00382-012-1446-5.

Danco, J. F., and E. R. Martin, 2018: Understanding the influence of ENSO on the Great Plains low-level jet in CMIP5 models. *Climate Dynamics*, **51 (4)**, 1537–1558, doi:10.1007/s00382-017-3970-9.

Deser, C., A. S. Phillips, and J. W. Hurrell, 2004: Pacific Interdecadal Climate Variability: Linkages between the Tropics and the North Pacific during Boreal Winter since 1900. *Journal of Climate*, **17 (16)**, 3109–3124, doi:10.1175/1520-0442(2004)017<3109:PICVLB>2.0.CO;2.

Deser, C., and K. Trenberth, 2016: The climate data guide: Pacific decadal oscillation (pdo): Definition and indices.". URL https://climatedataguide.ucar.edu/climate-data/pacific-decadal-oscillation-pdo-definition-and-indices.

Ding, Q., and B. Wang, 2005: Circumglobal teleconnection in the northern hemisphere summer. *Journal of Climate*, **18 (17)**, 3483–3505, doi:10.1175/JCLI3473.1.

Ding, Q., B. Wang, J. M. Wallace, and G. Branstator, 2011: Tropical–extratropical teleconnections in boreal summer: Observed interannual variability. *Journal of Climate*, **24 (7)**, 1878–1896, doi:10.1175/2011JCLI3621.1.

Dirmeyer, P. A., and K. L. Brubaker, 1999: Contrasting evaporative moisture sources during the drought of 1988 and the flood of 1993. *Journal of Geophysical Research: Atmospheres*, **104 (D16)**, 19 383–19 397, doi:10.1029/1999JD900222.

Dirmeyer, P. A., and J. L. Kinter III, 2009: The maya express: Floods in the u.s. midwest. *Eos, Transactions American Geophysical Union*, **90 (12)**, 101–102, doi:10.1029/2009EO120001.

Ferguson, C. R., S. Agrawal, M. C. Beauharnois, G. Xia, D. A. Burrows, and L. F. Bosart, 2020: Assimilation of satellite-derived soil moisture for improved forecasts of the Great Plains low-level jet. *Monthly Weather Review*, 1–64, doi:10.1175/MWR-D-20-0185.1.

Ferguson, C. R., M. Pan, and T. Oki, 2018: The effect of global warming on future water availability: Cmip5 synthesis. *Water Resources Research*, **54 (10)**, 7791–7819, doi:10.1029/2018WR022792.

Ferguson, C. R., and E. F. Wood, 2011: Observed land-atmosphere coupling from satellite remote sensing and reanalysis. *Journal of Hydrometeorology*, **12 (6)**, 1221–1254, doi: 10.1175/2011JHM1380.1.

Ghil, M., and Coauthors, 2002: Advanced spectral methods for climatic time series. *Reviews of Geophysics*, **40 (1)**, doi:10.1029/2000RG000092.

Good, S. A., M. J. Martin, and N. A. Rayner, 2013: En4: Quality controlled ocean temperature and salinity profiles and monthly objective analyses with uncertainty estimates. *Journal of Geophysical Research: Oceans*, **118 (12)**, 6704–6716, doi:10.1002/2013JC009067.

Hoerling, M., J. Eischeid, A. Kumar, R. Leung, A. Mariotti, K. Mo, S. Schubert, and R. Seager, 2014: Causes and predictability of the 2012 great plains drought. *Bulletin of the American Meteorological Society*, **95 (2)**, 269–282, doi:10.1175/BAMS-D-13-00055.1.

Hoerling, M., X.-W. Quan, and J. Eischeid, 2009: Distinct causes for two principal u.s. droughts of the 20th century. *Geophysical Research Letters*, **36 (19)**, doi:10.1029/2009GL039860.

Holton, J. R., 1967: The diurnal boundary layer wind oscillation above sloping terrain. *Tellus Series A*, **19 (2)**, 199–205, doi:10.1111/j.2153-3490.1967.tb01473.x.

Hu, Q., S. Feng, and R. J. Oglesby, 2011: Variations in North American Summer Precipitation Driven by the Atlantic Multidecadal Oscillation. *Journal of Climate*, **24 (21)**, 5555–5570, doi: 10.1175/2011JCLI4060.1.

Huang, C. S. Y., and N. Nakamura, 2016: Local finite-amplitude wave activity as a diagnostic of anomalous weather events. *Journal of the Atmospheric Sciences*, **73 (1)**, 211–229, doi: 10.1175/JAS-D-15-0194.1.

Hurrell, J. W., 1995: Decadal trends in the north atlantic oscillation: Regional temperatures and precipitation. *Science*, **269 (5224)**, 676–679, doi:10.1126/science.269.5224.676.

Hurrell, J. W., Y. Kushnir, G. Ottersen, and M. Visbeck, 2003: The north atlantic oscillation: Climatic significance and environmental impact. *Geophysical Monograph Series*, **134**, 1–35, doi:10.1029/2003EO080005.

Jiang, X., N.-C. Lau, and S. A. Klein, 2006: Role of eastward propagating convection systems in the diurnal cycle and seasonal mean of summertime rainfall over the u.s. great plains. *Geophysical Research Letters*, **33 (19)**, doi:10.1029/2006GL027022.

Joseph, P. V., and J. Srinivasan, 1999: Rossby waves in May and the Indian summer monsoon rainfall. *Tellus A*, **51 (5)**.

Kam, J., J. Sheffield, and E. F. Wood, 2014: Changes in drought risk over the contiguous united states (1901–2012): The influence of the pacific and atlantic oceans. *Geophysical Research Letters*, **41 (16)**, 5897–5903, doi:10.1002/2014GL060973.

Karmakar, N., A. Chakraborty, and R. Nanjundiah, 2017: Space–time evolution of the low- and high-frequency intraseasonal modes of the indian summer monsoon. *Monthly Weather Review*, **145 (2)**, 413–435, doi:10.1175/MWR-D-16-0075.1.

Keenlyside, N. S., M. Latif, and A. Dürkop, 2007: On Sub-ENSO Variability. *Journal of Climate*, **20 (14)**, 3452–3469, doi:10.1175/JCLI4199.1.

Koster, R. D., Y. Chang, H. Wang, and S. D. Schubert, 2016: Impacts of local soil moisture anomalies on the atmospheric circulation and on remote surface meteorological fields during boreal summer: A comprehensive analysis over north america. *Journal of Climate*, **29 (20)**, 7345–7364, doi:10.1175/JCLI-D-16-0192.1.

Krishnamurthy, L., G. A. Vecchi, R. Msadek, A. Wittenberg, T. L. Delworth, and F. Zeng, 2015: The seasonality of the great plains low-level jet and enso relationship. *Journal of Climate*, **28 (11)**, 4525–4544, doi:10.1175/JCLI-D-14-00590.1.

Krishnamurthy, V., and V. Misra, 2010: Observed enso teleconnections with the south american monsoon system. *Atmospheric Science Letters*, **11 (1)**, 7–12, doi:10.1002/asl.245.

Laloyaux, P., and Coauthors, 2018: Cera-20c: A coupled reanalysis of the twentieth century. *Journal of Advances in Modeling Earth Systems*, **10 (5)**, 1172–1195, doi:10.1029/2018MS001273.

Lau, K.-M., J.-Y. Lee, K.-M. Kim, and I.-S. Kang, 2004: The north pacific as a regulator of summertime climate over eurasia and north america. *Journal of Climate*, **17 (4)**, 819–833, doi:10.1175/1520-0442(2004)017<0819:TNPAAR>2.0.CO;2.

Lau, K.-M., and H. Weng, 2002: Recurrent teleconnection patterns linking summertime precipitation variability over east asia and north america. *Journal of the Meteorological Society of Japan. Ser. II*, **80 (6)**, 1309–1324, doi:10.2151/jmsj.80.1309.

Lavers, D., L. Luo, and E. F. Wood, 2009: A multiple model assessment of seasonal climate forecast skill for applications. *Geophysical Research Letters*, **36 (23)**, doi:10.1029/2009GL041365.

Li, L., W. Li, and Y. Kushnir, 2012: Variation of the north atlantic subtropical high western ridge and its implication to southeastern us summer precipitation. *Climate Dynamics*, **39 (6)**, 1401–1412, doi:10.1007/s00382-011-1214-y.

Li, Q., S. Yang, V. E. Kousky, R. W. Higgins, K.-M. Lau, and P. Xie, 2005: Features of cross-pacific climate shown in the variability of china and us precipitation. *International Journal of Climatology*, **25 (13)**, 1675–1696, doi:10.1002/joc.1271.

Liang, Y.-C., J.-Y. Yu, M.-H. Lo, and C. Wang, 2015: The changing influence of el niño on the great plains low-level jet. *Atmospheric Science Letters*, **16 (4)**, 512–517, doi:10.1002/asl.590.

Malloy, K. M., and B. P. Kirtman, 2020: Predictability of midsummer great plains low-level jet and associated precipitation. *Weather and Forecasting*, **35 (1)**, 215–235, doi:10.1175/WAF-D-19-0103.1.

Mantua, N. J., and S. R. Hare, 2002: The pacific decadal oscillation. *Journal of Oceanography*, **58 (1)**, 35–44, doi:10.1023/A:1015820616384.

Matsumura, S., and T. Horinouchi, 2016: Pacific ocean decadal forcing of long-term changes in the western pacific subtropical high. *Scientific Reports*, **6 (1)**, 37 765, doi:10.1038/srep37765.

Melillo, J. M., T. C. Richmond, and G. W. Yohe, 2014: Highlights of climate change impacts in the united states: the third national climate assessment. U.S. Global Change Research Program, http://dx.doi.org/10.7930/J08G8HMN.

Meng, L., and S. M. Quiring, 2010: Examining the influence of spring soil moisture anomalies on summer precipitation in the u.s. great plains using the community atmosphere model version 3. *Journal of Geophysical Research: Atmospheres*, **115 (D21)**, doi:10.1029/2010JD014449.

Mo, K. C., J.-K. E. Schemm, and S.-H. Yoo, 2009: Influence of ENSO and the Atlantic Multidecadal Oscillation on Drought over the United States. *Journal of Climate*, **22 (22)**, 5962–5982, doi:10.1175/2009JCLI2966.1.

Montini, T. L., C. Jones, and L. M. V. Carvalho, 2019: The south american low-level jet: A new climatology, variability, and changes. *Journal of Geophysical Research: Atmospheres*, **124 (3)**, 1200–1218, doi:10.1029/2018JD029634.

Newman, M., and Coauthors, 2016: The Pacific Decadal Oscillation, Revisited. *Journal of Climate*, **29 (12)**, 4399–4427, doi:10.1175/JCLI-D-15-0508.1.

Oglesby, R., S. Feng, Q. Hu, and C. Rowe, 2012: The role of the atlantic multidecadal oscillation on medieval drought in north america: Synthesizing results from proxy data and climate models. *Global and Planetary Change*, **84-85**, 56 – 65, doi:https://doi.org/10.1016/j.gloplacha.2011.07.005, perspectives on Climate in Medieval Time.

Parish, T. R., 2017: On the forcing of the summertime great plains low-level jet. *Journal of the Atmospheric Sciences*, **74 (12)**, 3937–3953, doi:10.1175/JAS-D-17-0059.1.

Plaut, G., and R. Vautard, 1994: Spells of low-frequency oscillations and weather regimes in the northern hemisphere. *Journal of the Atmospheric Sciences*, **51 (2)**, 210–236, doi:10.1175/1520-0469(1994)051<0210:SOLFOA>2.0.CO;2.

Ropelewski, C. F., and M. S. Halpert, 1986: North american precipitation and temperature patterns associated with the el niño/southern oscillation (enso). *Monthly Weather Review*, **114 (12)**, 2352–2362, doi:10.1175/1520-0493(1986)114<2352:NAPATP>2.0.CO;2.

Sardeshmukh, P. D., and B. J. Hoskins, 1988: The Generation of Global Rotational Flow by Steady Idealized Tropical Divergence. *Journal of the Atmospheric Sciences*, **45 (7)**, 1228–1251, doi:10.1175/1520-0469(1988)045<1228:TGOGRF>2.0.CO;2.

Schubert, S. D., M. J. Suarez, P. J. Pegion, R. D. Koster, and J. T. Bacmeister, 2004: On the cause of the 1930s dust bowl. *Science*, **303 (5665)**, 1855–1859, doi:10.1126/science.1095048.

Slivinski, L. C., and Coauthors, 2019: Towards a more reliable historical reanalysis: Improvements for version 3 of the twentieth century reanalysis system. *Quarterly Journal of the Royal Meteorological Society*, **145 (724)**, 2876–2908, doi:10.1002/qj.3598.

Tang, Y., S. Zhong, J. A. Winker, and C. K. Walters, 2016: Evaluation of the southerly low-level jet climatology for the central united states as simulated by narccap regional climate models. *International Journal of Climatology*, **36 (13)**, 4338–4357, doi:10.1002/joc.4636.

Teng, H., G. Branstator, H. Wang, G. A. Meehl, and W. M. Washington, 2013: Probability of us heat waves affected by a subseasonal planetary wave pattern. *Nature Geoscience*, **6 (12)**, 1056–1061, doi:10.1038/ngeo1988.

Thorne, P. W., and R. S. Vose, 2010: Reanalyses suitable for characterizing long-term trends. *Bulletin of the American Meteorological Society*, **91 (3)**, 353–362, doi:10.1175/2009BAMS2858.1.

Titchner, H. A., and N. A. Rayner, 2014: The met office hadley centre sea ice and sea surface temperature data set, version 2: 1. sea ice concentrations. *Journal of Geophysical Research: Atmospheres*, **119 (6)**, 2864–2889, doi:10.1002/2013JD020316.

Trenberth, K. E., 1997: The definition of el niño. *Bulletin of the American Meteorological Society*, **78 (12)**, 2771–2778, doi:10.1175/1520-0477(1997)078<2771:TDOENO>2.0.CO;2.

Trenberth, K. E., G. W. Branstator, and P. A. Arkin, 1988: Origins of the 1988 north american drought. *Science*, **242 (4886)**, 1640–1645, URL http://www.jstor.org/stable/1703393.

Trenberth, K. E., and D. J. Shea, 2006: Atlantic hurricanes and natural variability in 2005. *Geophysical Research Letters*, **33 (12)**, doi:10.1029/2006GL026894.

van den Hurk, B., F. Doblas-Reyes, G. Balsamo, R. D. Koster, S. I. Seneviratne, and H. Camargo, 2012: Soil moisture effects on seasonal temperature and precipitation forecast scores in europe. *Climate Dynamics*, **38 (1)**, 349–362, doi:10.1007/s00382-010-0956-2.

Wang, H., and S. Schubert, 2014: The precipitation response over the continental united states to cold tropical pacific sea surface temperatures. *Journal of Climate*, **27 (13)**, 5036–5055, doi:10.1175/JCLI-D-13-00453.1.

Wang, H., S. Schubert, M. Suarez, and R. Koster, 2010a: The physical mechanisms by which the leading patterns of sst variability impact u.s. precipitation. *Journal of Climate*, **23 (7)**, 1815–1836, doi:10.1175/2009JCLI3188.1.

Wang, H., S. D. Schubert, R. D. Koster, and Y. Chang, 2019: Phase locking of the boreal summer atmospheric response to dry land surface anomalies in the northern hemisphere. *Journal of Climate*, **32 (4)**, 1081–1099, doi:10.1175/JCLI-D-18-0240.1.

Wang, L., W. Chen, and R. Huang, 2008: Interdecadal modulation of pdo on the impact of enso on the east asian winter monsoon. *Geophysical Research Letters*, **35 (20)**, doi:10.1029/2008GL035287.

Wang, S.-Y., and T.-C. Chen, 2009: The late-spring maximum of rainfall over the u.s. central plains and the role of the low-level jet. *Journal of Climate*, **22 (17)**, 4696–4709, doi:10.1175/2009JCLI2719.1.

Wang, S.-Y., R. E. Davies, and R. R. Gillies, 2013: Identification of extreme precipitation threat across midlatitude regions based on short-wave circulations. *Journal of Geophysical Research (Atmospheres)*, **118 (19)**, 11,059–11,074, doi:10.1002/jgrd.50841.

Wang, S.-Y., L. E. Hipps, R. R. Gillies, X. Jiang, and A. L. Moller, 2010b: Circumglobal teleconnection and early summer rainfall in the us intermountain west. *Theoretical and Applied Climatology*, **102 (3)**, 245–252, doi:10.1007/s00704-010-0260-4.

Watanabe, T., and K. Yamazaki, 2014: Decadal-scale variation of South Asian summer monsoon onset and its relationship with the pacific decadal oscillation. *Journal of Climate*, **27 (13)**, 5163–5173.

Weaver, S. J., and S. Nigam, 2008: Variability of the great plains low-level jet: Large-scale circulation context and hydroclimate impacts. *Journal of Climate*, **21 (7)**, 1532–1551, doi: 10.1175/2007JCLI1586.1.

Weaver, S. J., S. Schubert, and H. Wang, 2009: Warm season variations in the low-level circulation and precipitation over the central united states in observations, amip simulations, and idealized sst experiments. *Journal of Climate*, **22 (20)**, 5401–5420, doi:10.1175/2009JCLI2984.1.

Wei, W., W. Li, Y. Deng, and S. Yang, 2019: Intraseasonal variation of the summer rainfall over the southeastern united states. *Climate Dynamics*, **53 (1)**, 1171–1183, doi: 10.1007/s00382-018-4345-6.

Whiteman, C. D., X. Bian, and S. Zhong, 1997: Low-level jet climatology from enhanced rawinsonde observations at a site in the southern great plains. *Journal of Applied Meteorology*, **36 (10)**, 1363–1376, doi:10.1175/1520-0450(1997)036<1363:LLJCFE>2.0.CO;2.

Woodruff, S. D., and Coauthors, 2011: Icoads release 2.5: extensions and enhancements to the surface marine meteorological archive. *International Journal of Climatology*, **31 (7)**, 951–967, doi:10.1002/joc.2103.

Xue, Y., R. Vasic, Z. Janjic, Y. M. Liu, and P. C. Chu, 2012: The impact of spring subsurface soil temperature anomaly in the western u.s. on north american summer precipitation: A case study using regional climate model downscaling. *Journal of Geophysical Research: Atmospheres*, **117 (D11)**, doi:10.1029/2012JD017692.

Xue, Y., and Coauthors, 2016: Spring land temperature anomalies in northwestern US and the summer drought over southern plains and adjacent areas. *Environmental Research Letters*, **11 (4)**, 044 018, doi:10.1088/1748-9326/11/4/044018.

Xue, Y., and Coauthors, 2018: Spring land surface and subsurface temperature anomalies and subsequent downstream late spring-summer droughts/floods in north america and east asia. *Journal of Geophysical Research: Atmospheres*, **123 (10)**, 5001–5019, doi:10.1029/2017JD028246.

Yang, S., X. Ding, D. Zheng, and Q. Li, 2007: Depiction of the variations of great plains precipitation and its relationship with tropical central-eastern pacific sst. *Journal of Applied Meteorology and Climatology*, **46 (2)**, 136–153, doi:10.1175/JAM2455.1.

Yu, L., S. Zhong, X. Bian, and W. E. Heilman, 2015: Temporal and Spatial Variability of Wind Resources in the United States as Derived from the Climate Forecast System Reanalysis. *Journal of Climate*, **28 (3)**, 1166–1183, doi:10.1175/JCLI-D-14-00322.1.

Zhou, F., R. Zhang, and J. Han, 2020: Influences of the east asian summer rainfall on circumglobal teleconnection. *Journal of Climate*, **33 (12)**, 5213–5221, doi:10.1175/JCLI-D-19-0325.1.

Zhu, Z., and T. Li, 2016: A new paradigm for continental u.s. summer rainfall variability: Asia–north america teleconnection. *Journal of Climate*, **29 (20)**, 7313–7327, doi:10.1175/JCLI-D-16-0137.1.

LIST OF TABLES

TABLE 1. Years constituting the upper (Q4) and lower (Q1) quartiles of May SCP coupled (LLJC) and uncoupled (LLJUC) low-level jet frequency years.

LLJ Quartiles	Years
Q4 LLJC	1960 1955 1917 2010 1950 2002 1938 1990 1944 2008 1982 1961 1983 1903 1975 1956 1946 1959 1981 1971 1965 1918 1916 1942 1953 1962 1991 1977
Q1 LLJC	1910 2009 1997 1904 1924 1934 1928 1940 1925 1931 1996 1901 2001 1920 1963 2000 1966 1952 1936 1941 1937 1994 1914 1973 1919 1969 1939 1935
Q4 LLJUC	1941 2009 1905 1989 1939 1962 1956 1921 1931 2006 1952 1929 1940 2004 1908 1984 1904 1902 1964 1914 1911 1970 1945 1910 1963 2000 1996 1934
Q1 LLJUC	1953 1983 1980 1982 1977 1922 1991 1955 1981 1947 1975 1968 1946 1971 1916 1957 2005 1942 1995 1999 1903 1976 1909 1924 1973 1917 1954 1960

TABLE 2. Pearson's r (r^2) between May SCP total (LLJT), coupled (LLJC), and uncoupled (LLJUC) low-level jet frequencies and A) CGT (all 110 years), CGT|+PDO, CGT|-PDO; B) the Pacific Ocean SST-based climate indices for the period from 1901-2010, C) the Atlantic Ocean climate indices. Values are computed from the CERA20C ensemble mean dataset. Correlation coefficients significant at the $\alpha = 0.1$ level are emboldened. Refer to Sec. 2e for details about the significance test.

A) Jet class	LLJT	LLJC	LLJUC
CGT	0.15 (0.02)	**0.62** (0.38)	**-0.48** (0.23)
CGT|+PDO	-0.02 (0.00)	**0.56** (0.31)	**-0.54** (0.29)
CGT|-PDO	**0.27** (0.07))	**0.68** (0.46)	**-0.41** (0.17)

B) Jet class	LLJT	LLJC	LLJUC
Niño3.4 May	**-0.19** (0.04)	-0.11 (0.01)	-0.08 (0.01)
Niño3.4 JFM	**-0.22** (0.05)	-0.05 (0.00)	**-0.17** (0.03)
Niño4 May	**-0.22** (0.05)	-0.12 (0.01)	-0.1 (0.01)
Niño4 JFM	**-0.24** (0.05)	-0.06 (0.00)	**-0.18** (0.03)
PDO May	-0.12 (0.01)	**-0.22** (0.05)	0.09 (0.01)

C) Jet class	LLJT	LLJC	LLJUC
NAO May	**0.23** (0.05)	-0.09 (0.01)	**0.33** (0.11)
NASH May	0.07 (0.00)	-0.15 (0.02)	**0.23** (0.05)
AMO	0.01 (0.00)	-0.03 (0.00)	0.04 (0.00)

TABLE 3. Pearson's correlation of May area-averaged CERA-20C ensemble mean 0600 UTC Z250 between the four CGT centers of action (i.e., R1-R4; Fig. 6c) during 1901-2010. Correlation coefficients significant at the $\alpha = 0.1$ level are emboldened.

CGT-center	R1: West Asia	R2: East Asia	R3: East N. Pacific	R4: West U.S.
R1	1	**-0.29**	**0.24**	-0.13
R2	**-0.29**	1	-0.12	**0.23**
R3	**0.24**	-0.12	1	**-0.33**

LIST OF FIGURES

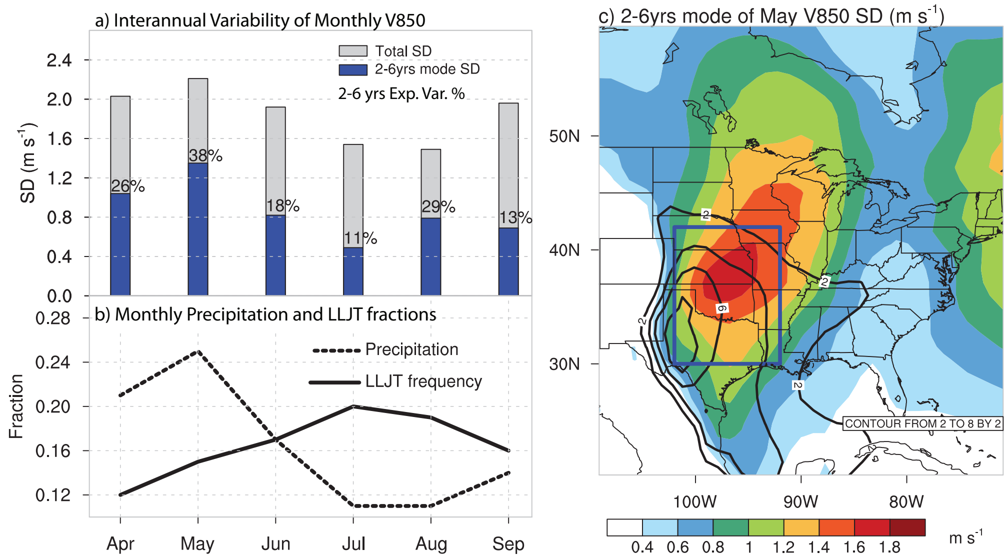

FIG. 1. a) Interannual standard deviation (SD; m s^{-1}) of monthly 850-hPa meridional wind (V850; in gray) and of its filtered 2-6 year oscillating component (blue) for the South Central Plains (SCP; 102°-92° W, 30°-42° N; blue box in 1c). Percentage of total variance explained by the 2-6 year oscillatory mode is notated. b) Monthly total LLJ frequency (LLJT, solid line) and precipitation (dashed line) over SCP as a fraction of warm-season totals. c) SD of filtered 2-6 years oscillatory mode in May V850 (m s^{-1}) in color and mean May V850 (m s^{-1}) contours in black.

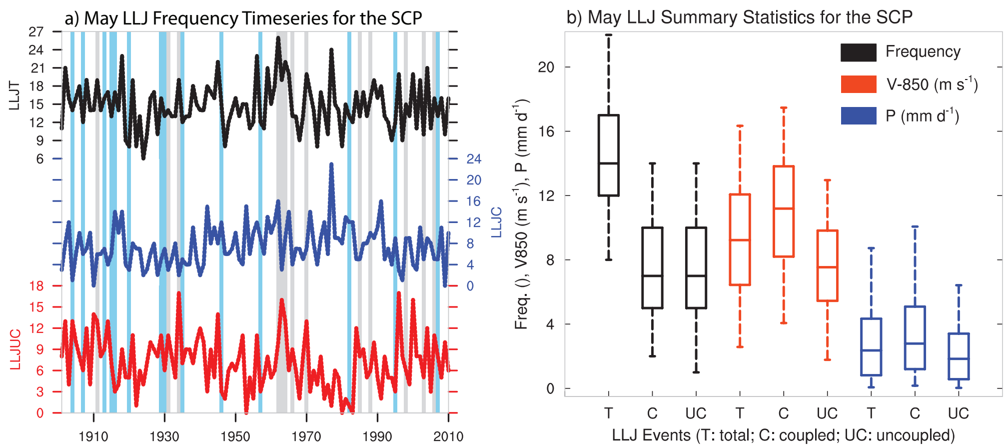

FIG. 2. a) May frequencies of total (LLJT; black), coupled (LLJC; blue), and uncoupled (LLJUC; red) LLJs for the period from 1901-2010. Sky blue bars denote years with positive May precipitation anomalies and gray bars denote years with negative May precipitation anomalies in the SCP. b) Box plot of 1901-2010 mean May LLJ frequency (d; black), 0600 UTC V850 (m s^{-1}; red), and precipitation (Prec, mm d^{-1}; blue) for the SCP. Only active LLJ days are used in the calculation of the V850 and Prec means. Prec means are 24 h accumulated, centered around 0600 UTC. Box plot whiskers extend to 5^{th} and 95^{th} percentiles.

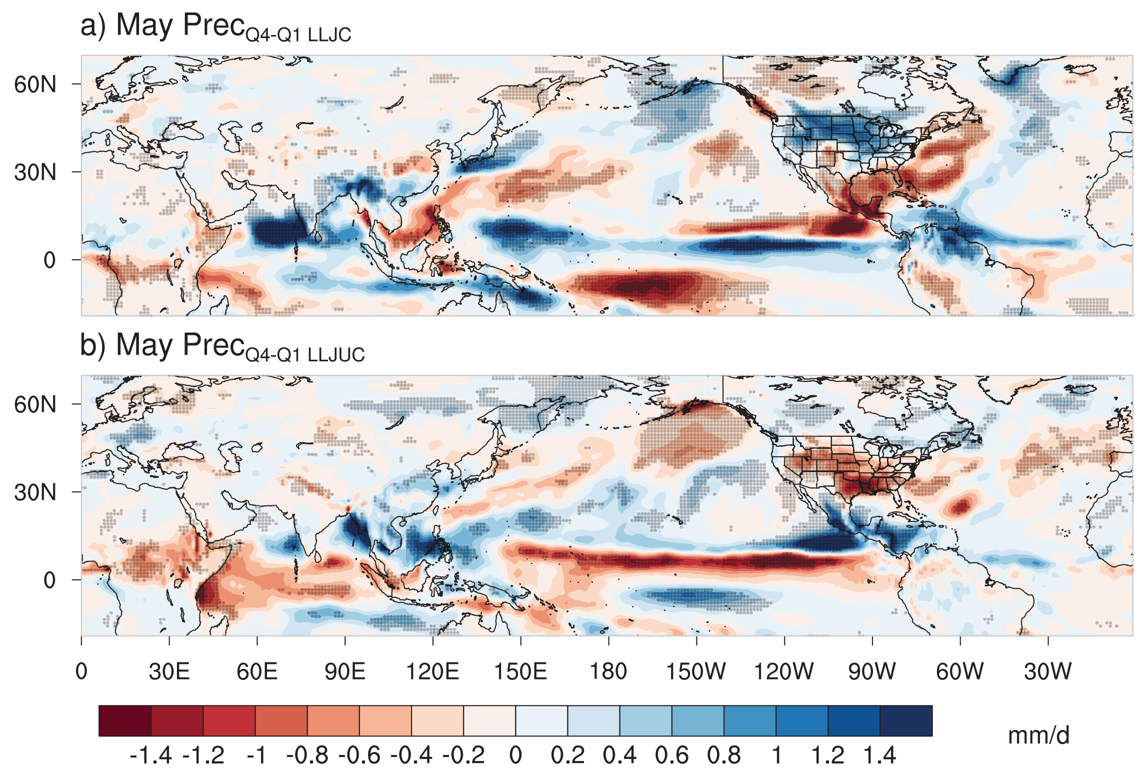

FIG. 3. Composite differences of May 24-hour accumulated precipitation (Prec; mm d^{-1}) between upper and lower quartiles of a) LLJC and b) LLJUC frequency years. Differences are computed, for example, by subtracting mean precipitation of the first quartile (0-25%) of LLJC (LLJUC) frequency years from mean precipitation of the fourth quartile (75-100%) of LLJC (LLJUC) frequency years (hereafter, Q4-Q1 composite). Q4-Q1 composite differences that are significant at $\alpha = 0.1$ are stippled. Refer to Sec. 2d for details about the significance test.

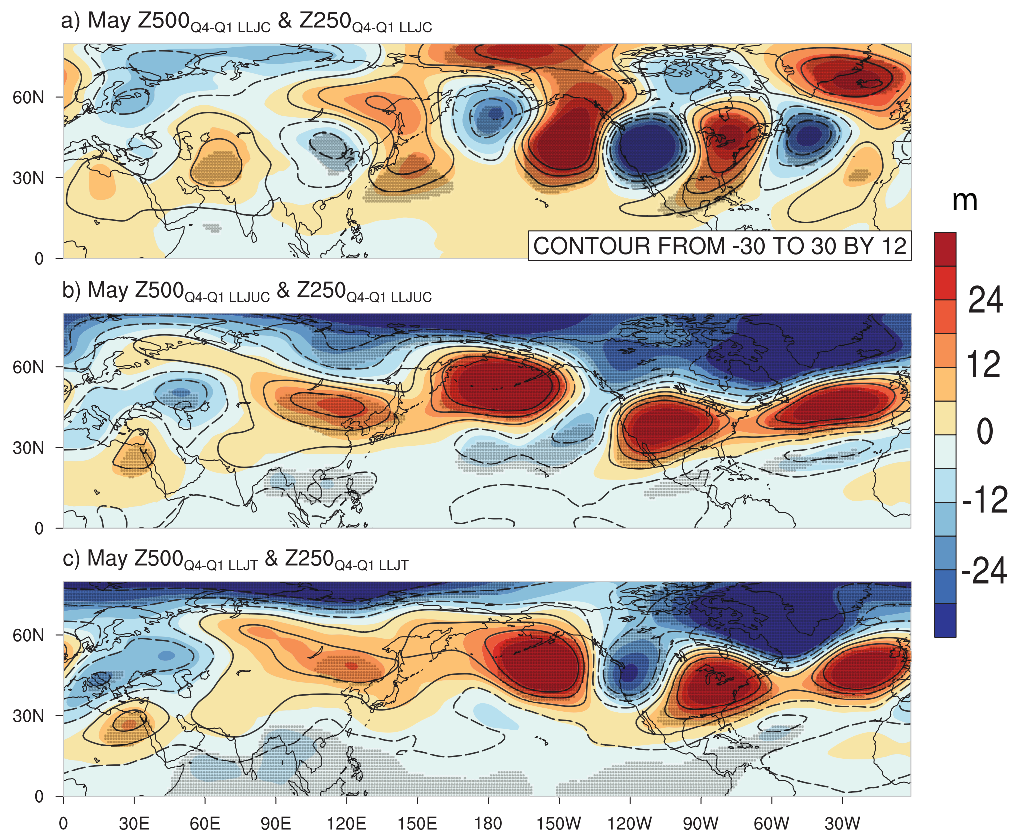

FIG. 4. Q4-Q1 of May 0600 UTC Z500 (m, shaded; colors are by 6) and Z250 (m, contoured; contours are by 12; solid: positive, dashed: negative) for a) LLJC , b) LLJUC, and c) LLJT years. Z500 Q4-Q1 composite differences that are significant at $\alpha = 0.1$ are stippled.

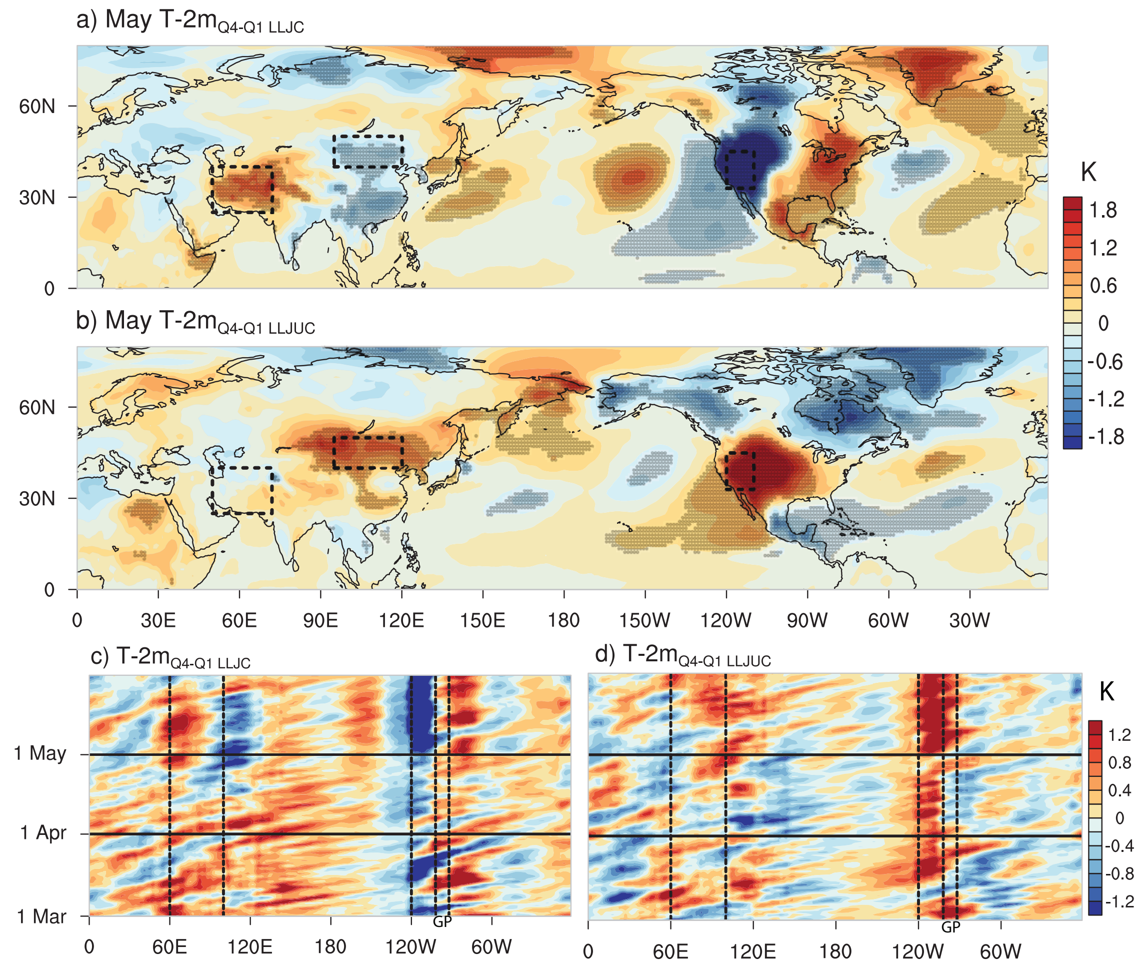

FIG. 5. Q4-Q1 a, c) LLJC and b, d) LLJUC composites for a-b) May 2m air temperature (T-2m; K) and c-d) March 1^{st}- May 31^{st} daily mean T-2m. Differences significant at $\alpha = 0.1$ are stippled in a-b. Select continental regions with significant T-2m differences in (a) are focused with dashed boxes. Hovmöller diagrams (c-d) are for daily T-2m differences averaged over 25°-50° N. Dashed vertical lines are drawn at 60° E, 100° E, 120° W, and 102°-92° W (SCP boundaries).

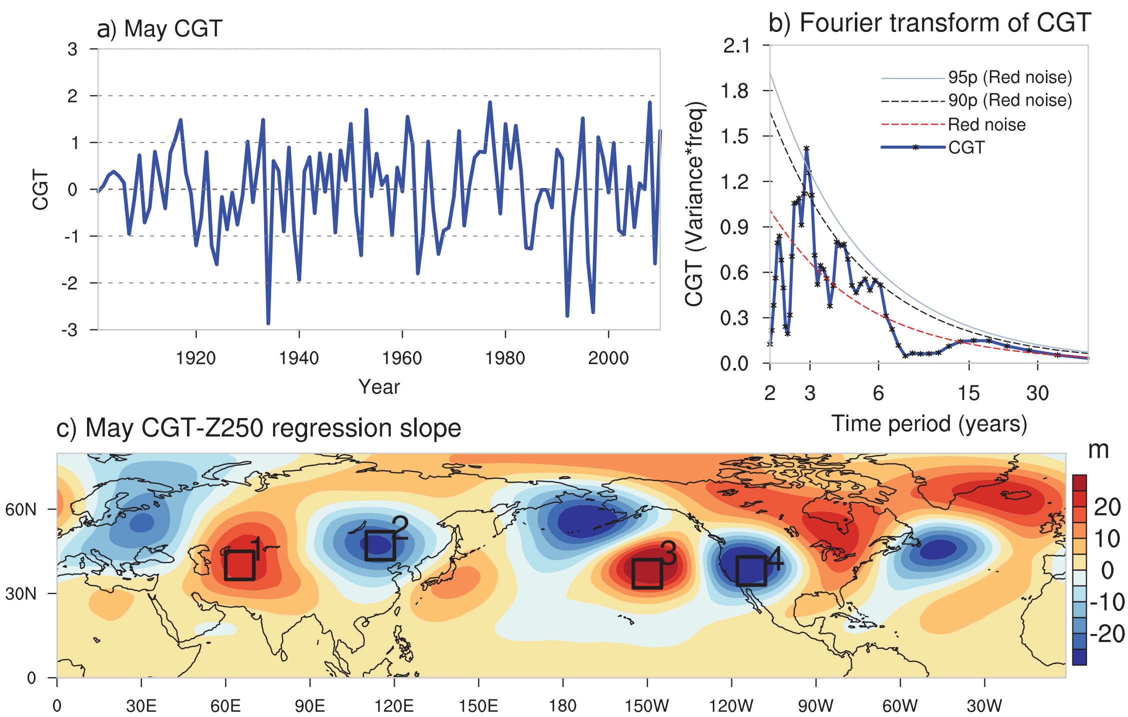

FIG. 6. a) The time series of May CGT computed for 1901-2010. b) Fourier transform of the May 1901-2010 CGT index (blue), red noise spectrum (red) and its 90^{th} percentile (black) and 95^{th} percentile (gray) bounds. c) May CGT regressed with May 0600 UTC Z250 (m). The regions used to define CGT are boxed (i.e., [Z250[1] + Z250[3] - Z250[2] -Z250[4]]/SD(CGT)). Refer to Sec. 2.e.1 for details.

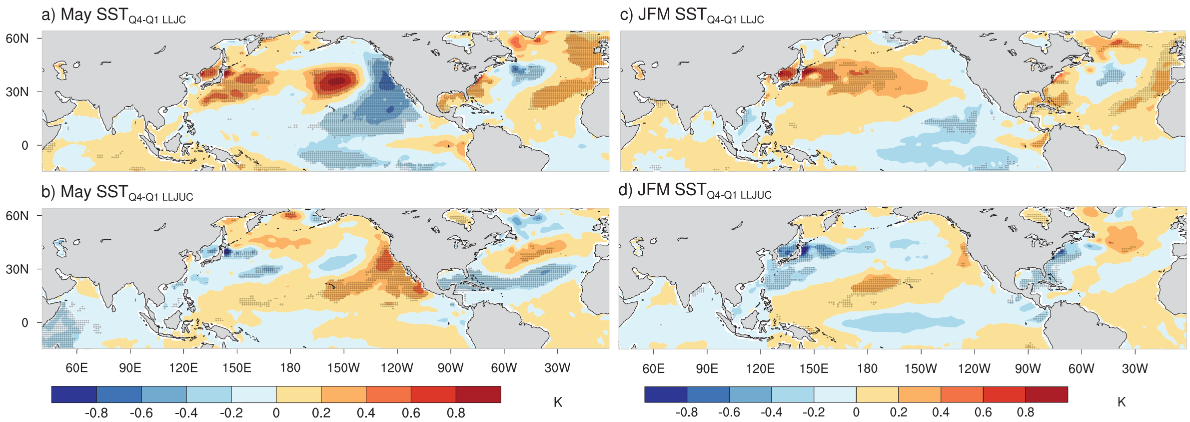

FIG. 7. Q4-Q1 composites of SSTs (K) in May and preceding winters (Jan-Feb-Mar; JFM) for May SCP LLJC and LLJUC. a) May SSTs Q4-Q1 LLJC, b) May SSTs Q4-Q1 LLJUC, c) JFM SSTs Q4- Q1 LLJC, and d) JFM SSTs Q4-Q1 LLJUC. SST differences significant at $\alpha = 0.1$ are stippled.

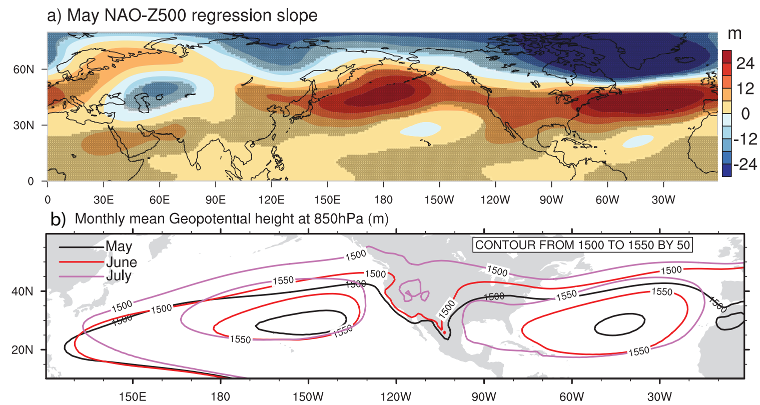

1061 FIG. 8. a) May NAO regressed with May 0600 UTC Z500 (m). Regression coefficients significant at $\alpha = 0.1$
1062 are stippled. b) Monthly mean Z850 (m) for May (black), June (red), and July (orchid). Only the 1500 m and
1063 1550 m contours are drawn.

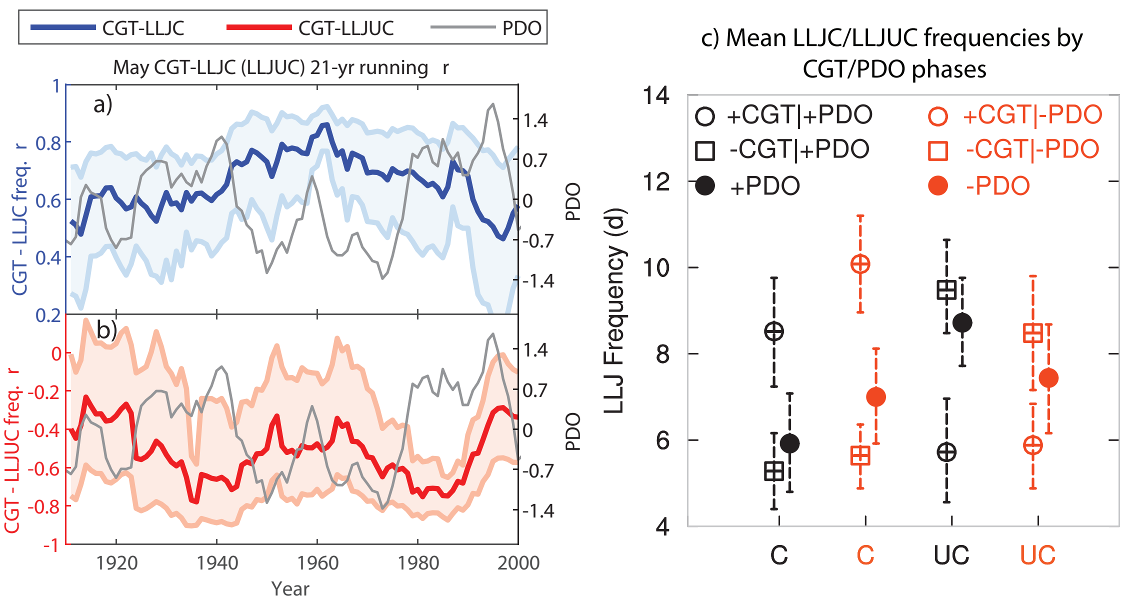

FIG. 9. a) 21-year running window correlation between May CGT and SCP LLJC frequency (a; blue); May CGT and SCP LLJUC frequency (b; red). Correlation values (r) are plotted at the center year of the 21-year window. Shades represent the 90% confidence intervals of r values from 10,000-bootstrapped samples of 21-year window. In addition, the 10-year running mean of the May PDO index (black) is superimposed in (a-b). Refer to Sec. 2.e.2 for the PDO index. c) May SCP LLJC and LLJUC frequency means during positive PDO (black) and negative PDO (red) years. Solid circles show the mean LLJ frequency for all +PDO or -PDO years. Open circle and square markers show mean LLJ frequency conditioned on +CGT and -CGT years, in addition to PDO phases. Whiskers show the 90% confidence intervals of frequency means from 10,000-bootstrapped samples of each set of years conditioned on CGT and PDO phases. Refer to Table S1 for constituent years.

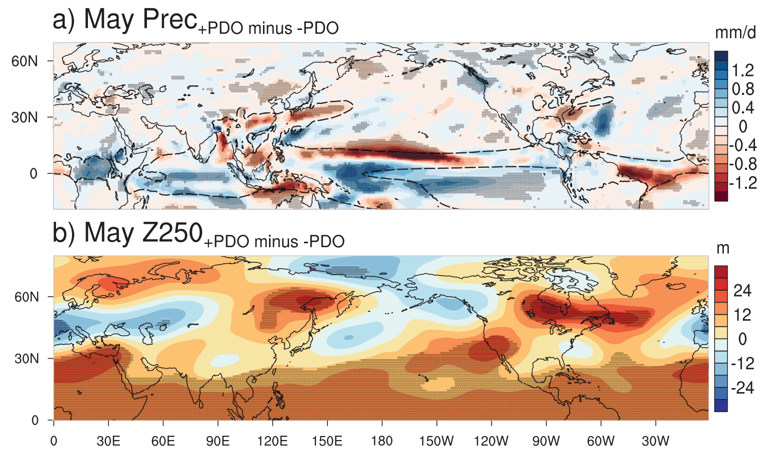

1073 Fig. 10. a) Composite differences of May 24-hour accumulated precipitation (Prec; mm d^{-1}) between $+PDO$
1074 and $-PDO$ years. The dashed black line shows the climatological mean 4 mm d^{-1} precipitation contour for May.
1075 b) Same as a), but for May 0600 UTC Z250 (m). Composite differences significant at $\alpha = 0.1$ are stippled.

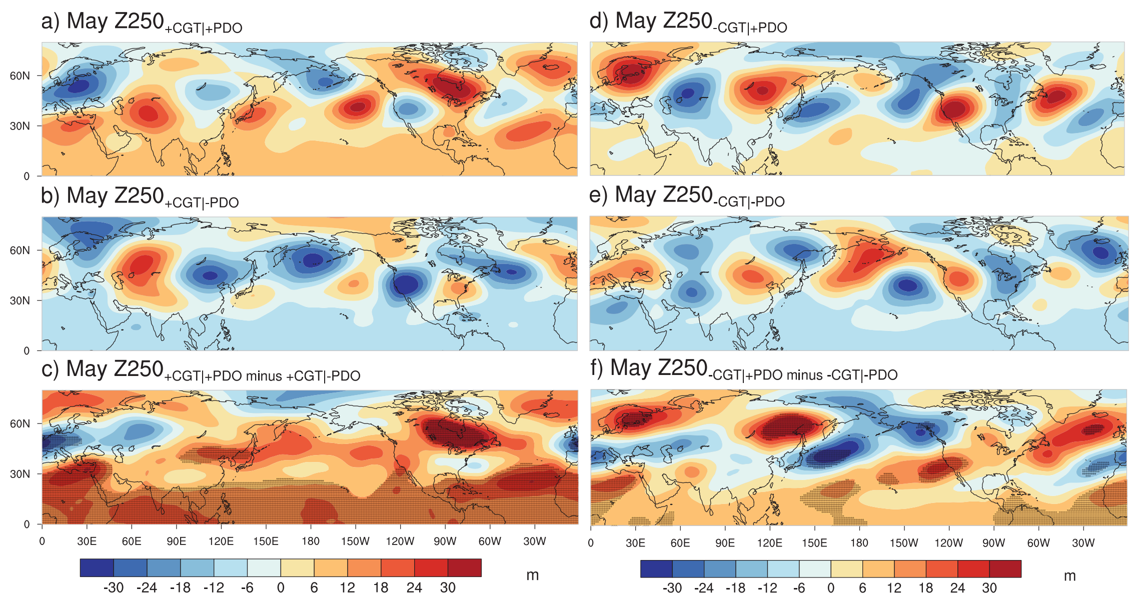

FIG. 11. a-b, d-e) Composite means of May 0600 UTC Z250 (m) anomalies computed by subtracting the 110-year mean at each grid. a) $+CGT|+PDO$ years, b) $+CGT|-PDO$ years, d) $-CGT|+PDO$ years, and e) $-CGT|-PDO$ years. c & f) Composite differences of May 0600 UTC Z250 (m) between c) $+CGT|+PDO$ minus $+CGT|-PDO$ (e.i. a-b); f) $-CGT|+PDO$ minus $-CGT|-PDO$ (e.i. d-e). Composite differences significant at $\alpha = 0.1$ are stippled in c & f. Refer to Table S1 for constituent years.

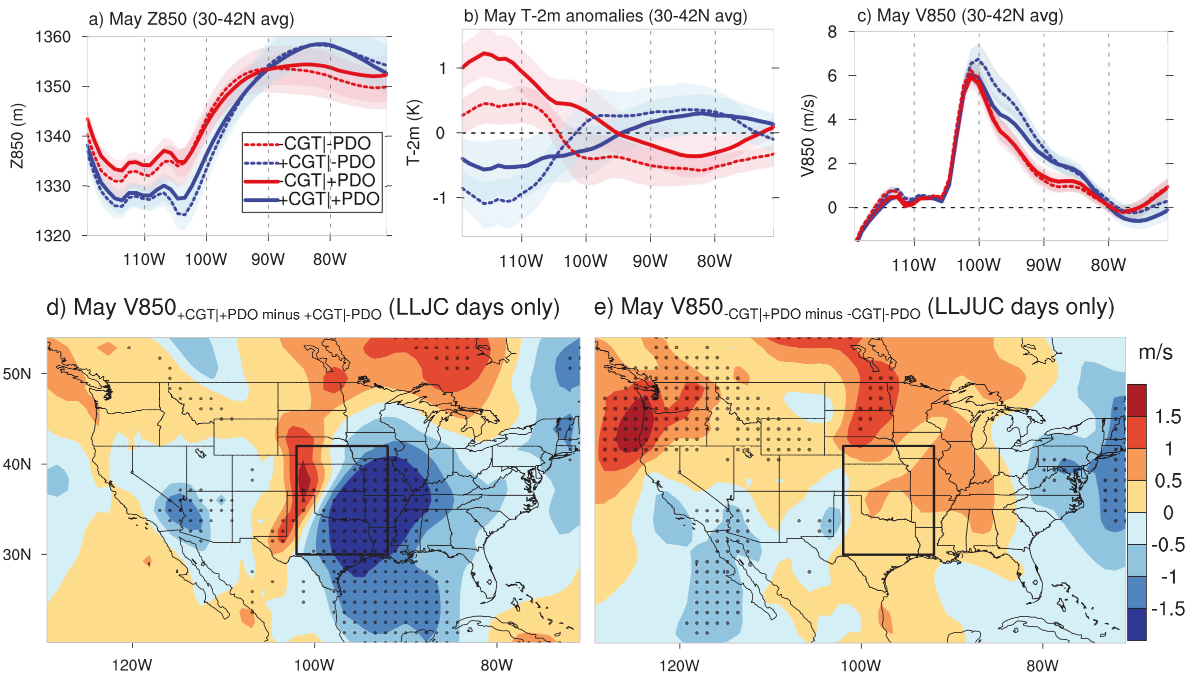

FIG. 12. a) May 0600 UTC Z850 (m) averaged over 30°-42° N for +CGT|+PDO years (soild blue), -CGT|+PDO years (soild red), +CGT|-PDO years (dashed blue), and -CGT|-PDO years (dashed red). b) May T-2m anomalies (K) averaged over 30°-42° N for the same four composites of years as in (a). T-2m anomalies are computed by subtracting the climatological mean at each grid. c) May 0600 UTC V850 (m s^{-1}) averaged over 30°-42° N for the same four composites of years as in (a). Shades in a-c represent the 90% confidence intervals of the means from 10,000-bootstrapped samples of 25-year subsets. d-e) Composite differences of May 0600 UTC V850 (m s^{-1}) for d) +CGT|+PDO minus +CGT|-PDO years considering LLJC days only, and e) -CGT|+PDO minus -CGT|-PDO years considering LLJUC days only. V850 differences significant at $\alpha = 0.1$ are stippled. Refer to Table S1 for constituent years.